



Contents lists available at ScienceDirect

International Journal of Plasticity

journal homepage: www.elsevier.com/locate/ijplas



A hydrogen diffusion model considering grain boundary characters based on crystal plasticity framework

Kaidi Li^a, Bin Tang^{a,b,*}, Mengqi Zhang^a, Liguo Zhao^{c,d,**}, Xudong Liu^a, Jiangkun Fan^a, Jinshan Li^{a,b,*}

^a State Key Laboratory of Solidification Processing, Northwestern Polytechnical University, Xi'an 710072, China

^b Chongqing Innovation Center, Northwestern Polytechnical University, Chongqing 401135, China

^c College of Energy and Power Engineering, Nanjing University of Aeronautics and Astronautics, Nanjing 210016, China

^d Wolfson School of Mechanical, Electrical and Manufacturing Engineering, Loughborough University, Loughborough LE11 3TU, UK



ARTICLE INFO

Keywords:

Hydrogen embrittlement
Grain boundary
Crystal plasticity
Hydrogen transportation
Segregation energy
Hydrostatic stress

ABSTRACT

The influence of grain boundaries (GBs) on hydrogen transportation is a crucial factor in understanding the mechanisms of hydrogen embrittlement (HE) in polycrystalline alloys. Crystal plasticity models have the advantages in simulating the effect of grain microstructure on hydrogen diffusion in polycrystals, but they have not yet been coupled with hydrogen diffusion models that can take into account GB characters. In this study, a hydrogen diffusion model that considers the effect of GBs on the transportation of hydrogen was developed to study the local hydrogen diffusion behavior in bi-crystalline and polycrystalline alloys. The simulation results showed the capability of the model in describing the influence of hydrogen on the material deformation. In addition, this study found that the hydrostatic stress determined the hydrogen concentration in the far-GB region, whereas the GB energy played a control role in and near the GB regions. Notably, hydrogen exhibits a preference for localization near high-angle grain boundaries (HAGBs) and triple junctions. In alloys with medium grain size, hydrogen typically had low average concentration with a more uniform distribution. Furthermore, the hydrogen-assisted crack growth mechanism was analyzed as the continuous coalescence of primary and secondary cracks along GBs. This work presents a hydrogen diffusion model that considers GB effects, and the proposed model has advantages in predicting the deformation and fracture of polycrystalline alloys in hydrogen environments.

1. Introduction

To mitigate global warming, the transition towards zero-emission energy systems is imperative (Davis et al., 2018). Hydrogen, a clean energy source with high energy density and abundant reserves, has garnered considerable attention (Bayrakdar Ates and Calik, 2023; Cecere et al., 2014; Maugh, 1972). However, the ingress of hydrogen atoms can result in the degradation of the mechanical properties of materials exposed to a hydrogen atmosphere, a phenomenon referred as hydrogen embrittlement (HE), which

* Corresponding authors at: State Key Laboratory of Solidification Processing, Northwestern Polytechnical University, Xi'an 710072, China.

** Corresponding author at: College of Energy and Power Engineering, Nanjing University of Aeronautics and Astronautics, Nanjing 210016, China.

E-mail addresses: toby@nwpu.edu.cn (B. Tang), L.Zhao@nuaa.edu.cn (L. Zhao), ljsh@nwpu.edu.cn (J. Li).

significantly affects the storage, transportation, and widespread application of hydrogen energy (Huang et al., 2017; Johnson, 1973). To facilitate the utilization of hydrogen energy, numerous studies have been conducted to elucidate the underlying mechanisms of HE phenomenon and to develop novel alloys with superior resistance to HE.

The extreme small size of hydrogen atoms makes it difficult to experimentally capture their specific distribution within materials. Common experimental methods include: (i) thermal desorption spectroscopy (TDS) analysis (Claeys et al., 2020; Ohaeri et al., 2018), which provides macroscopic information on the average desorption rate of hydrogen but obscures effects of microstructures such as grain boundaries (GBs) and dislocations on hydrogen distribution; (ii) hydrogen microprint technique such as silver decoration technique used by Ohaeri et al. (2018) to capture the distribution of hydrogen in pure iron and determine the microstructure sensitivity of hydrogen diffusion; (iii) atom probe tomography (APT) used by Chen et al. (2020) to investigate the 3D distribution characteristics of hydrogen in steel, especially hydrogen atoms trapped at dislocations and GBs. To date, several well-established mechanisms of HE have been identified, including hydrogen-enhanced decohesion (HEDE) (Pfeil, 1926), hydrogen-enhanced localized plasticity (HELP) (Birnbaum; and Sofronis, 1994; Murakami and Matsuoka, 2010; Takakuwa et al., 2017), adsorption-induced dislocation-emission (AIDE) (Lynch, 1988, 1989, 2009), and hydrogen-enhanced strain-induced vacancies (Nagumo and Takai, 2019). The interplay and synergistic effects of these mechanisms collectively dictate the failure behaviours of materials (Djukic et al., 2019). However, due to experimental limitations and high research costs, the fundamental mechanism of HE remains incompletely understood, and represents a topic requiring further research efforts. The development and design of HE-resistance alloys still face significant challenges.

In recent years, the advancement of numerical simulation techniques has partly compensated for the difficulty of experimental studies on material deformation and hydrogen diffusion behaviors. Atomistic/molecular-scale simulations can replicate the complex interaction between hydrogen atoms and GB structures in details, such as density functional theory (Tehranchi and Curtin, 2017), first-principles calculations (Alvaro et al., 2015; Di Stefano et al., 2015; Jiang and Carter, 2004), cohesive models (Olden et al., 2008; Yu et al., 2017), molecular dynamics models (Song and Curtin, 2013; Zhou et al., 2021), and Monte Carlo simulations (Ramasubramaniam et al., 2011; Solanki et al., 2012; Song and Curtin, 2011). However, atomistic-scale simulations require models containing hundreds or thousands of atoms, which have high computational costs and can only simulate for the picosecond time range. This makes the method unsuitable for simulating the effect of grain microstructure on hydrogen diffusion in polycrystals.

Continuum methods, such as mesoscale crystal plasticity model and macroscopic finite element simulations, possess advantages in simulating hydrogen diffusion behavior at grain and component levels (Abdolvand, 2019). In particular, Darken and Smith (1949) proposed that hydrogen would be trapped by defects in materials, and McNabb and Foster (1963) developed a mathematical method to account for hydrogen trapping in metals. Based on these work, Oriani (1970) concluded that local hydrogen concentration should satisfy an equilibrium state. These early works greatly contributed to the technical progress and breakthroughs in hydrogen diffusion simulations. Sofronis and McMeeking (1989) investigated the diffusion behavior of hydrogen near a blunting crack tip of iron using finite element method, and identified the driving factors and distribution characteristics of hydrogen transportation. Subsequently, their group carried out a series of studies on HE (Lufrano and Sofronis, 1996; Lufrano et al., 1996, 1998; Taha and Sofronis, 2001). To simulate hydrogen diffusion behavior computationally, Oh et al. (2010) integrated the model in Sofronis and McMeeking (1989) into the ABAQUS software using the heat analogy method. In the same year, Miresmaeli et al. (2010) coupled the crystal plasticity model with the hydrogen diffusion model, which further advanced the development of hydrogen diffusion simulation. Barrera et al. (2016) and Díaz et al. (2016) investigated the hydrogen diffusion behavior at the crack or notch tip. Following a similar approach, Fernández-Sousa et al. (2020) investigated the behavior of hydrogen trapped at dislocations, carbides, and martensite interfaces under fatigue loading using a similar approach, providing guidance for the development of alloys that are resistant to hydrogen-induced fatigue failure. Elmukashfi et al. (2020) employed the finite element method and discovered that the hydrogen concentration within the lattice is governed by hydrostatic stress (HS). However, upon stress relaxation, there exists a phenomenon where hydrogen atoms near the GBs tend to escape from the interface. Taking the advantage of crystal plasticity in modeling microstructure-dependent local deformation, Ilin et al. (2014) investigated the distribution of hydrogen in stainless steel caused by stress and strain heterogeneity, and suggested that the accumulation of hydrogen atoms was promoted by the high level of HS, especially near the GBs. Abdolvand (2019) considered the precipitation and dissolution kinetics of δ -hydrides in the diffusion model, and studied the distribution characteristics of δ -hydrides in Zircaloy-2 alloy. Subsequently, his team conducted research on the hydrogen accumulation behavior in the vicinity of zirconium hydrides and the influence of the microstructural characteristics on the hydrogen diffusion behavior at the notch tip (Tondro and Abdolvand, 2021, 2022). Kumar et al. (2019) introduced a fatigue indicator parameter into the coupled model to study the evolution of fatigue damage behavior in polycrystalline nickel in hydrogen environment. Arnaudov et al. (2020) used accumulated plastic strain as a fatigue indicator parameter to predict the fatigue crack initiation lifetime in ferritic stainless steel subjected to HE. Recently, Yuan et al. (2022) considered both first-order and second-order hydrogen diffusion and investigated hydrogen diffusion behavior in polycrystalline pure nickel. They suggested that second-order hydrogen diffusion during deformation lead to hydrogen atom enrichment near the GBs. Simulation results in Tondro et al. (2023) revealed that there is a high concentration of hydrogen in the vicinity of GBs, with particularly exacerbated conditions observed at triple junctions. Furthermore, the effects of hydrogen on dislocation multiplication and annihilation have also been studied using crystal plasticity simulations (Singh et al., 2022). According to these studies, the preferential diffusion and segregation of hydrogen on or near GBs are the key factors in hydrogen-induced cracking (Li et al., 2019), but they have not been properly considered in their respective numerical models.

In a study by Koyama et al. (2017), the effect of GB misorientation on hydrogen diffusion in pure iron was investigated using the silver decoration method. The findings suggested that GB misorientation was a key factor for the non-uniform distribution of hydrogen in the material, with a significantly lower concentration of hydrogen atoms at low-angle grain boundaries (LAGBs) when compared to high-angle grain boundaries (HAGBs). McC Carroll et al. (2022) employed APT to identify that hydrogen atoms tend to segregate near

high-energy GBs in low-carbon martensitic steel. Additionally, pure nickel is a typical material that is highly sensitive to hydrogen environment, exhibiting embrittlement failure via a brittle fracture mechanism along GBs in the presence of hydrogen (Alvaro et al., 2015; Tehranchi et al., 2020). Ma et al. (2018, 2021) employed scanning Kelvin probe force microscopy (SKPFM) to investigate the effect of different GB characters on hydrogen diffusion. The study concluded that the coherent $\Sigma 3$ twin boundary acts as a fast diffusion pathway for hydrogen, whereas random GBs did not exhibit any significant acceleration effect in hydrogen diffusion. Ogawa et al. (2020) conducted hydrogen assisted fatigue crack growth tests and found that hydrogen, whether internal or external, induced fatigue cracks to propagate along GBs in IN718 alloy. Cracks propagated primarily along HAGBs under external hydrogen conditions, while along HAGBs and twin boundaries under internal hydrogen conditions. Mai et al. (2021) employed first-principle calculations and found that special high-coherent GBs with low excess volume and low energy are significantly less favorable for hydrogen segregation and accumulation, whereas high-energy GBs and random boundaries exhibit the opposite behavior. Furthermore, Díaz et al. (2019) used finite element method and discovered that the fraction of the random GBs and misorientation angles have a significant impact on the hydrogen trapping and short-circuit diffusion characteristics. These findings suggest that the diffusion of hydrogen is governed by the GB properties. Therefore, it is essential to consider the GB characters in the model for investigating hydrogen diffusion in polycrystalline materials as well as for developing HE-resistant alloys.

Motivated by the aforementioned research gaps, this study developed an innovative model for hydrogen diffusion in the polycrystalline materials. Coupled with crystal plasticity, the model aims to simulate hydrogen diffusion along the GBs of different characters, with a particular encompass of hydrogen trapping and detrapping processes at the GBs. Based on this model, the factors influencing hydrogen distribution near [100] symmetric tilt grain boundaries (STGBs) were first investigated for a bicrystal, followed by analysis of hydrogen diffusion behavior in a polycrystal. Specifically, Section 2 elaborates on the crystal plasticity constitutive model employed in this study, along with the development of hydrogen diffusion constitutive model. Section 3 provides the relevant details of the computer model utilized in this study. Section 4 conducts a thorough analysis of hydrogen diffusion behavior for pure nickel with a respective bicrystal and polycrystalline microstructure, including the calibration of constitutive model parameters. And Section 5 finishes this paper with main conclusions.

2. Model description

In this study, all non-italicized bold symbols represent tensor, italicized bold symbols represent matrix, and italicized non-bold symbols represent scalars.

2.1. Crystal plasticity constitutive model

A rate-dependent crystal plasticity constitutive model is adopted in this study, and it incorporates the evolution of the stored statistically dislocations (SSDs) and geometrically necessary dislocations (GNDs) due to plastic strain gradients at geometrically incompatible locations (Ashby, 1970), such as GBs. The deformation gradient can be decomposed into elastic and plastic parts:

$$\mathbf{F} = \mathbf{F}^e \cdot \mathbf{F}^p \quad (1)$$

where \mathbf{F}^e is the elastic deformation gradient caused by the lattice stretch and crystal rigid rotation, \mathbf{F}^p refers to the dislocation slip on the slip systems. The plastic velocity gradient is described by the shear strain rate on each slip system as:

$$\mathbf{L}^p = \dot{\mathbf{F}}^p \mathbf{F}^{p-1} = \sum_{\alpha=1}^N \dot{\gamma}^\alpha \mathbf{s}_0^\alpha \otimes \mathbf{n}_0^\alpha \quad (2)$$

where \mathbf{s}_0^α and \mathbf{n}_0^α are the slip direction and normal of the slip plane of the α -th slip system, respectively. The inelastic strain rate, $\dot{\gamma}^\alpha$, for each slip system can be expressed by:

$$\dot{\gamma}^\alpha = \dot{\gamma}_0 \left| \frac{\tau^\alpha}{g^\alpha} \right|^n \operatorname{sgn}(\tau^\alpha) \quad (3)$$

in which the resolved shear stress τ^α is given by the Schmid's law. The slip resistance g^α includes the contribution of both the SSDs and GNDs, and is described by a Taylor-type multi-slip hardening equation as:

$$g^\alpha = \alpha_0 \mu b \sqrt{\sum_{\beta=1}^N A^{\alpha\beta} (\rho_{SSD}^\beta + \rho_{GND}^\beta)} \quad (4)$$

where α_0 , μ , and b are a dimensionless parameter, shear modulus, and Burger's vector, respectively. $A^{\alpha\beta}$ in the strength-interaction matrix between the dislocations on all slip systems. ρ_{SSD}^β and ρ_{GND}^β are the density of SSDs and GNDs in the β -th slip system, respectively. GBs are one of the key factors influencing material deformation. Moghaddam et al. (2017) and Zhang et al. (2022) found that such interfaces can introduce additional strengthening effects to the material, manifested in the form of an influence zone, which arises from the overlapping Laue patterns between adjacent grains (Chandra et al., 2020). Therefore, an extra strengthening term g_{HP} named the averaged strength of GB region is introduced into the Eq. (4) to describe the effect of the GBs on the deformation of bicrystal and

polycrystalline models:

$$g^\alpha = \alpha_0 \mu b \sqrt{\sum_{\beta=1}^N A^{\alpha\beta} (\rho_{SSD}^\beta + \rho_{GND}^\beta)} + g_{HP} \quad (5)$$

For the sake of simplicity, the initial strength of GB region, referred to as g_{HP} , is assumed to be independent of both the misorientation and GB energy. Detailed explanations regarding this decision can be found in [Appendix A](#).

The evolution of the SSDs density is described as:

$$\dot{\rho}_{SSD}^\alpha = \frac{1}{b} \left(\frac{1}{L^\alpha} - k_b \rho_{SSD}^\alpha \right) |\dot{\gamma}^\alpha| \quad (6)$$

where k_b is the dynamic recovery coefficient relating to the annihilation distance between dislocations and is expressed as:

$$k_b = \frac{1}{2} (y_e + y_s) \quad (7)$$

in which y_e refers to the annihilation distance between edge dislocations and approximated by $6b$ in FCC metals ([Martinez-Mardones et al., 2000](#)). In the case of screw dislocations, annihilation distance is described as y_s , depends on ability of screw dislocations to cross-slip. For nickel, y_s is assumed to be 26.5 nm according to the results by dislocation dynamics simulations ([Pauš et al., 2013](#)). L^α is the dislocation mean free path (MFP) of the α -th slip system:

$$L^\alpha = -\frac{K}{\sqrt{\sum_{\beta=1}^N H^{\alpha\beta} (\rho_{SSD}^\beta + \rho_{GND}^\beta)}} \quad (8)$$

where K is the athermal hardening coefficient, $H^{\alpha\beta}$ is the average segment length-interaction matrix represents the mutual immobilization between dislocations, and have a similar form with $A^{\alpha\beta}$ in [Eq. \(4\)](#).

As described in [Anahid et al. \(2011\)](#), the contribution of GNDs to the slip resistance can also be expressed as:

$$\Delta g_{GNDs}^\alpha = \frac{\alpha_0^2 \mu^2 b}{2g^\alpha} \sum_\beta^{Nslip} \lambda^\beta |\dot{\gamma}^\beta| \quad (9)$$

where λ^β is a measure of the slip plane lattice incompatibility and can be expressed as a function of the slip plane normal \mathbf{n}^β and Nye tensor Λ ([Nye, 1953](#)):

$$\lambda^\beta = (\Lambda \mathbf{n}^\beta : \Lambda \mathbf{n}^\beta)^{1/2} \quad (10)$$

and the Nye tensor can be expressed by the curl of the plastic deformation gradient \mathbf{F}^p :

$$\Lambda = \nabla^T \times \mathbf{F}^p \quad (11)$$

The slip resistance stems from SSDs can also be expressed as ([Han et al., 2015](#); [Li et al., 2021](#); [Roters et al., 2010](#); [Zhang et al., 2022](#)):

$$g^\alpha = \sum_\beta^{Nslip} h_{\alpha\beta} |\dot{\gamma}^\beta| \quad (12)$$

By partitioning the model into two regions, GB region and grain interior (GI) region, and combining the [Eq. \(12\)](#) with [Eqs. \(4\)–\(6\)](#), [\(8\)](#), and [\(9\)](#), the hardening modulus $h_{\alpha\beta}$ in [Eq. \(12\)](#) can be described as:

$$h_{\alpha\beta} = \begin{cases} \frac{\alpha_0^2 \mu^2 b}{2g^\alpha} A^{\alpha\beta} \left(\frac{1}{L^\beta} - k_b \rho_{SSD}^\beta + \frac{k_0 \lambda^\beta}{A^{\alpha\beta}} \right) & (\text{GIregion}) \\ \frac{\alpha_0^2 \mu^2 b}{2(g^\alpha - g_{HP})} A^{\alpha\beta} \left(\frac{1}{L^\beta} - k_b \rho_{SSD}^\beta + \frac{k_0 \lambda^\beta}{A^{\alpha\beta}} \right) & (\text{GBregion}) \end{cases} \quad (13)$$

Numerous existing studies have found that hydrogen may cause an increase in the yield stress of the materials, e.g. pure nickel ([Boniszewski and Smith, 1963](#)), pure aluminum ([Watson et al., 1988](#)) and stainless steel ([West and Louthan, 1982](#)), as a result of the hydrogen-dislocation interactions. Hence, the influence of the hydrogen on the evolution of the slip resistance is introduced into [Eq. \(4\)](#), where C_{D-H}^α is the current hydrogen concentration on the α -th slip system, and T_c is a parameter governing the hydrogen effect on the slip resistance ([Díaz et al., 2016](#); [Kumar et al., 2019](#)):

$$g_H^\alpha = (1 + T_c C_{D-H}^\alpha) g^\alpha \quad (14)$$

In addition, the results in literature ([Abraham and Altstetter, 1994](#); [Boniszewski and Smith, 1963](#)) show that hydrogen leads to the extra hardening effect during the plastic deformation. Thus, [Eq. \(13\)](#) is modified as:

$$h_{\alpha\beta,H} = (1 + H_c C_{D-H}^\alpha) h_{\alpha\beta} \quad (15)$$

where H_c is a parameter controlling the hardening caused by hydrogen (Schebler, 2010).

2.2. Hydrogen diffusion model

Solute hydrogen atoms occupy interstitial lattice sites and diffuses between them, but can also be trapped at sites such as GBs, free surfaces, vacancies, and dislocation cores (Chen et al., 2020). In the context of crystal plasticity, the diffusion of hydrogen is sensitive to the grain orientation and GBs type. Therefore, a quasi-physics-based diffusion model was proposed, which assumes that in the GI region, hydrogen atoms are present at normal interstitial lattice sites (NILS-H) and dislocation cores (D-H), while in the GB region, hydrogen atoms are present at GB trapping sites (GB-H) and the stored dislocation cores (D-H), as shown in Fig. 1(a2) and (a3).

The explanation of some variables and their symbols is as follows:

C_{D-H} , hydrogen concentration in dislocations cores [H atoms/mm³]

C_L , hydrogen concentration in normal interstitial lattice sites [H atoms/mm³]

C_{GB-H} , hydrogen concentration in GB region [H atoms/mm³]

C_{total} , total hydrogen concentration at each material point; for the GI region, $C_{total} = C_L + C_{D-H}$, and for the GB region, $C_{total} = C_{GB-H} + C_{D-H}$ [H atoms/mm³]

$C_{Averaged}$, the predicted value obtained from the Gaussian distribution of C_{total}

m , an index refers to different types of hydrogen

ω , an index refers to different regions

2.2.1. Mass balance equation of hydrogen

The concentration of NILS-H, D-H, and GB-H is expressed identically as the function of the sites per unit volume N_m and occupancy fraction θ_m (Sofronis and McMeeking, 1989):

$$C_m = N_m \theta_m \quad (16)$$

where m refers to three types of hydrogen. For NILS-H, the subscripts in Eq. (16) are written as "L", and the subscripts of other types of hydrogen remain unchanged.

For NILS-H and GB-H, it is assumed that the site concentration is constant during the deformation; the former is related to the atomic weight and density, and the latter is measured in the work (Lu et al., 2022b). For D-H, the site concentration evolves with the deformation of the material and comprises of 12 parts, each being a function of the dislocation density on each slip system. They are

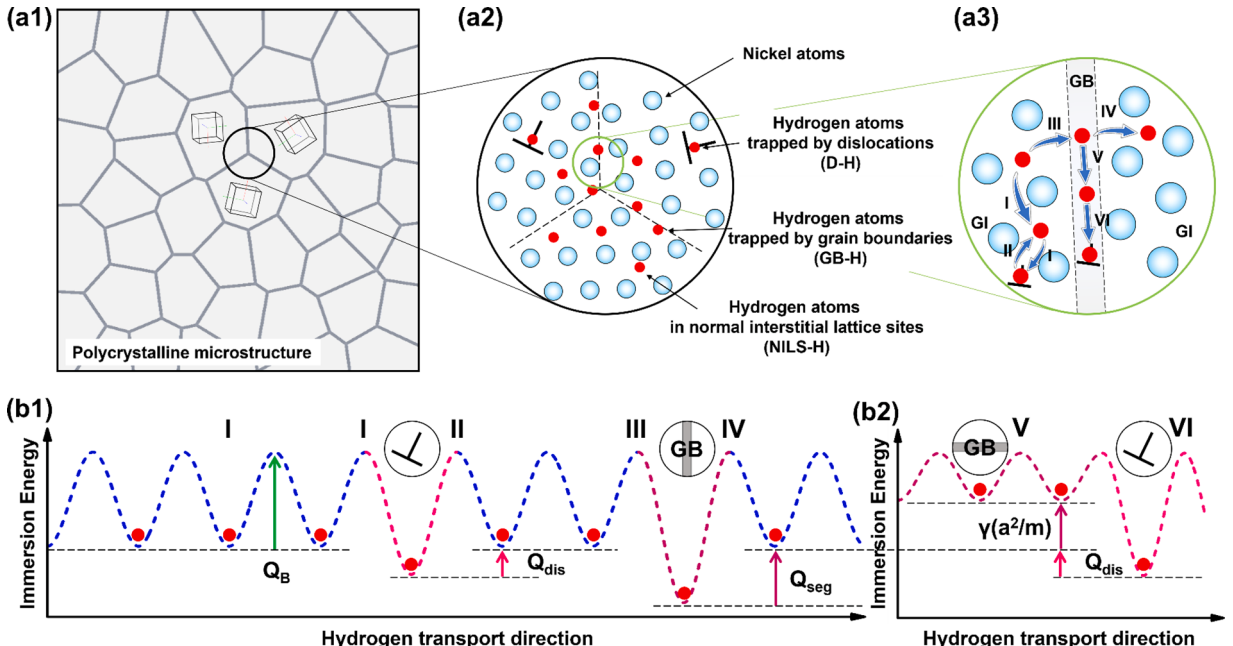


Fig. 1. Diagram of hydrogen transport: (a1)-(a3) hydrogen distribution and transport path; (b1)-(b2) dependence of hydrogen potential energy on the diffusion direction and location.

expressed as follows:

$$N_L = \frac{\beta_M N_A \rho_M}{M_M} \quad (17)$$

$$N_{D-H} = \sum_a^N N_{D-H}^a = \frac{\sqrt{2}}{a} \sum_a^N (\rho_{SSD}^a + \rho_{GND}^a) \quad (18)$$

where β_M is typically taken to be 1 in the case of FCC nickel, and N_A is the Avogadro's number. N_L is calculated to be 9.134×10^{19} H atoms/mm³ ($\rho_M = 8.902 \times 10^3$ kg/m³, $M_M = 58.69 \times 10^{-3}$ kg/mol for nickel).

The Oriani's equilibrium equation describes the relationship between the C_{D-H} and both the C_L and C_{GB-H} (Oriani, 1970):

$$\frac{\theta_{D-H}^a}{1 - \theta_{D-H}^a} \frac{1 - \theta_L}{\theta_L} = K_{D-H,NILS-H} = \exp\left(-\frac{Q_{dis}}{RT}\right) \quad (19)$$

$$\frac{\theta_{D-H}^a}{1 - \theta_{D-H}^a} \frac{1 - \theta_{GB-H}}{\theta_{GB-H}} = K_{D-H,GB-H} = \exp\left(-\frac{Q_{dis} - \gamma_{GB}(\hat{a}^2/\hat{m})}{RT}\right) \quad (20)$$

where R and T are the gas constant and absolute temperature in Kelvin, respectively. γ_{GB} is the GB energy, \hat{a} is the average equilibrium distance between atoms in the GB, \hat{m} is the number of atomic layers in GB. And K_{ij} represents the equilibrium constant between hydrogen species "i" and "j".

Combining the Eq. (19) and Eq. (20) yields the equilibrium relationship between GB-H and NILS-H. However, as the detrapping behavior of hydrogen atoms from GB trapping sites is influenced by the segregation energy rather than the GB energy, the equilibrium equation can be expressed as follows:

$$\frac{\theta_L}{1 - \theta_L} \frac{1 - \theta_{GB-H}}{\theta_{GB-H}} = \exp\left(-\frac{Q_{seg}}{RT}\right) \quad (21)$$

The energy terms inside the exponent of Eqs. (19)–(21) are detailed in the next Section.

Considering a body volume V with surface S , the rate of change of total hydrogen concentration inside V can be written by using the mass conservation law:

$$\frac{\partial}{\partial t} \int_V C_{total} dV + \int_S \mathbf{J} \cdot \mathbf{n} dS = 0 \quad (22)$$

where \mathbf{n} is an outward-pointing unit normal vector and \mathbf{J} denotes the hydrogen flux.

The hydrogen flux can be express as:

$$\mathbf{J}_\omega = -\mathbf{D}_\omega \left(\nabla C_\omega - \frac{C_\omega \bar{V}_H}{RT} \nabla \sigma_H \right) \quad (23)$$

where ω is an index that refers to different regions (L for GI region, and $GB-H$ for GB region). D_ω is the diffusion tensor for hydrogen atom at each material point, and for the GB region, it comprises two components forms, $D_{GB,\perp}$ and $D_{GB,\parallel}$, which respectively govern the diffusion of hydrogen perpendicular to the GB region and along the GB region, ∇C_L and $\nabla \sigma_H$ are the hydrogen concentration gradient and HS gradient, respectively. \bar{V}_H is the partial molar volume. The detailed derivation of Eq. (23) can be found from Díaz et al. (2016). By combining Eqs. (16) and (19)–(23), the equilibrium equation of hydrogen diffusion can be expressed as:

$$D_{eff} \frac{dC_\omega}{dt} + \theta_{D-H}^a \frac{dN_{D-H}^a}{d(\rho_{SSD}^a + \rho_{GND}^a)} \frac{d(\rho_{SSD}^a + \rho_{GND}^a)}{dt} + \nabla \cdot \mathbf{J}_\omega = 0 \quad (24)$$

$$D_{eff} = \left\{ \sum_{a=1}^{Nsip} \frac{N_{D-H}^a K_{D-H,\omega}^a N_\omega}{[N_\omega + C_L(K_{D-H,\omega}^a - 1)]^2} + 1 \right\} \quad (25)$$

2.2.2. Hydrogen transport in polycrystalline material

The diffusivity of hydrogen atoms in polycrystalline material is influenced by the microstructural features. The modified hydrogen diffusion model is demonstrated in Fig. 1, where each grain in the polycrystalline aggregate has a unique shape and orientation, resulting in a specific spatial orientation and disorientation of each GB (Fig. 1(a1)). Distribution diagrams of NILS-H, D-H, and GB-H are presented in Fig. 1(a2), indicating distinct diffusion behaviors, as elaborated in Fig. 1(a3), which can be classified into six diffusion modes as described below.

Type I: hydrogen atom diffuses freely in the lattice or diffuses to the dislocation cores. Hydrogen diffusivity satisfies the Arrhenius equation $D = D_0 \exp(-Q/kT)$, which is controlled by the temperature and the activated energy of each type of sites. It's assumed that the

hydrogen diffusion in nickel lattice is isotropic (Mehrer, 2007), and the diffusion tensor D_L in the GI region can be expressed as:

$$\mathbf{D}_L = D_s \mathbf{I} = D_{0_B} \exp\left(-\frac{Q_B}{k_B T}\right) \cdot \mathbf{I} \quad (26)$$

where D_s is the diffusion coefficient of hydrogen atoms in nickel lattice, and the function of pre-exponential constant D_{0_B} and activation energy Q_B for the lattice (Fig. 1(b1)). k_B is the Boltzmann constant, and \mathbf{I} is the identity tensor.

When the H-atom diffuses near the dislocations, it tends to diffuse into the zone of higher HS around the dislocation core, and this process does not need to overcome additional energy barriers, as type I shown in Fig. 1(b1). Therefore, the diffusion coefficient for H-atom to jump into the dislocation core is the same as that for the diffusion in the lattice.

Type II: hydrogen atoms escape from the dislocation cores. The potential energy of D-H in GI region is less than that of NILS-H, and it takes more energy for hydrogen atoms to jump into the lattice sites than lattice diffusion (Type II in Fig. 1(b1)). And this extra energy Q_{dis} is called the dislocation binding energy. In the crystal plasticity simulation, dislocations density at each integration point is stored in the form of state variable, and there will be two types of hydrogen, NILS-H and D-H, at the same integration point. Therefore, the Oriani's equilibrium relation (Eq. (19)) is used to describe the behavior of D-H jumping out of the dislocation core into the lattice sites. And the equilibrium coefficient $K_{TD-H, NILS-H}$ is calculated based on Q_{dis} in Eq. (19).

Type III: hydrogen atoms diffuse to GBs. The diffusion barrier for hydrogen atoms jumping into GB trapping sites is equivalent to the lattice diffusion activation energy, and does not require overcoming additional potential energies, as described in Iljin et al. (2016). Consequently, the diffusion coefficient of this process is the same as that of the lattice diffusion.

Type IV: hydrogen atoms escape from the GBs. The GB-H has a lower potential energy than D-H as the specific structure and property of GBs. It is more difficult for GB-H to jump from GBs trapping sites into lattice sites because of the segregation energy Q_{seg} of GB (Iljin et al., 2016), and the diffusion coefficient of this process can be expressed as:

$$D_{GB,\perp} = D_{0_B} \exp\left(-\frac{Q_B - Q_{seg}}{k_B T}\right) \quad (27)$$

where Q_{seg} is negative and related to the GB character.

Type V: hydrogen atoms diffuse along GBs. In FCC materials, GBs may act as preferential paths for hydrogen diffusion, so called short circuit paths. Moghadam et al. (2015) substituted the diffusion equation $D = D_0 \exp(-Q/k_B T)$ into the Borisov relation to study the effects of GB character on mass transport in polycrystals. The developed equation is:

$$\gamma_{GB} = \left(\frac{1}{\kappa \hat{a}^2}\right) \left[k_B T \ln\left(\frac{D_{0_{GB}}}{D_{0_B}}\right) + (Q_B - Q_{GB}) \right] \quad (28)$$

where κ is the constant determined by the diffusion type (1: interstitial diffusion; 2: vacancy-assisted diffusion). $D_{0_{GB}}$ and Q_{GB} are the pre-exponential constant and activation energy for the GB, respectively.

Page et al. (2021) related GB diffusion to the GB energy and modified Eq. (28) into:

$$\frac{\gamma_{GB}}{k_B T} = \left(\frac{\hat{m}}{\hat{a}^2}\right) \left[\ln\left(\frac{D_{GB}}{D_B}\right) - \ln\lambda \right] \quad (29)$$

By substituting the bulk diffusivity equation, Eq. (29) can be rearranged as:

$$D_{GB,\parallel} = \lambda D_{0_B} \exp\left(-\frac{Q_B - \gamma(\hat{a}^2/\hat{m})}{k_B T}\right) \quad (30)$$

where λ is a positive constant that relates to the specific property of the GB. Therefore, Eq. (30) means that the diffusivity of hydrogen along the GB is higher than that between lattice sites due to the effect of the GB energy.

Type VI: GB-H atoms are trapped by the dislocations stored in the GB region. Research shows that the intrinsic dislocations stored in the GB region of nickel act as the trapping sites for GB-H, and it may weaken the diffusivity of GB-H transport along the GB (Yao and Chaoon, 1991). The intrinsic dislocations in the GB is assumed to only accommodate the grain misorientations (Ashby, 1970; Nye, 1953). And Oudriss et al. (2012) verified that GNDs seem to represent irreversible traps for hydrogen. As shown in Fig. 1(b2), D-H atoms in GB region need to overcome a higher potential energy barrier compared to those in the GI region to escape from the dislocation trapping sites. Therefore, the diffusion coefficient of GB-H atoms jumping out of the trapping sites of GNDs can be expressed as:

$$D_{D-GB} = D_{0_B} \exp\left(-\frac{Q_B - Q_{dis} - \gamma_{GB}(\hat{a}^2/\hat{m})}{k_B T}\right) \quad (31)$$

The Oriani's equilibrium equation is used to describe the trapping effect of GNDs on GB-H (Eq. (20)).

The above hydrogen diffusion types are all incorporated in the current model and also summarized in Table 1.

The effect of GB orientation and misorientation on diffusion is incorporated into Eq. (23). Fig. 2 illustrates a schematic diagram of three grains and their GBs. The misorientation, Δg_{12} and Δg_{23} , are calculated based on the Euler angles of the two grains sharing the GBs. The GB energies for nickel GBs with different misorientations, is obtained from Olmsted et al. (2009). Assuming that a GB region makes an angle, θ_G , with the global coordinate X-axis, the diffusion tensor for this GB regions in the local coordinate system of GB is multiplied by the rotation matrix, R, as given by Eq. (32), to obtain the diffusion tensor, D_{global} , in the global coordinate system. When θ_G is 90°, the local coordinate system of GB coincides with the global coordinate system.

$$\mathbf{D}_{global} = |\mathbf{R} \cdot \mathbf{D}_{local}| = \left| \begin{bmatrix} \sin\theta_G & \cos\theta_G & 0 \\ -\cos\theta_G & \sin\theta_G & 0 \\ 0 & 0 & 1 \end{bmatrix} \cdot \begin{bmatrix} D_{GB,\perp} \\ D_{GB,\parallel} \\ D_{GB,\parallel} \end{bmatrix} \right| \quad (32)$$

It should be noted that there are no externally imposed artificial interface conditions between the GB region and GI region, hereinafter referred to as the GIGB interface. The interface conditions between these regions are already implicitly incorporated in the constitutive model mentioned above. At the GIGB interface, the additional slip resistance of the GB region to dislocations results in significant stress and strain gradients, similar to the results reported in Haouala et al. (2018). This also leads to discontinuous HS between the two grains (Liu and Sluiter, 2023). Therefore, the jump in the gradient of HS is implicitly satisfied. Regarding the hydrogen diffusion process, the diffusion at the GIGB interface is controlled by the hydrogen diffusion flux represented by Eq. (23), which is mainly influenced by the gradients of HS and the diffusion tensor during isothermal processes. As for the diffusion tensor, it is dependent on the current position of the hydrogen atom. In the GI region, hydrogen diffusion is related to the activation energy Q_B for the lattice, while the hydrogen diffusion flux in the GB region is influenced by the GB energy γ_{GB} and segregation energy Q_{seg} . When the hydrogen flux is perpendicular to GB, it is primarily governed by Q_{seg} , while along GB, it is influenced by the GB energy. Therefore, the distinct diffusion characteristics in the GI region and GB region have implicitly differentiate their roles in the hydrogen diffusion process.

2.3. Numerical implementation

Elements in the GB region are actually similar to that within GI region but possess GB strength and diffusion characteristics. In the finite element solution process, no special treatment is applied to the elements in the GB and GI regions, and a consistent approach is employed. In this manner, the continuity of the chemical potential can be achieved across the elements in the GB region, and the numerical problems may arise if this continuity cannot be maintained (Elmukashfi et al., 2020).

The numerical representation of the single crystal constitutive model in Section 2.1 was implemented by a quasi-implicit forward gradient times integration algorithm developed by Peirce et al. (1983). And the crystal plasticity model was coded into a user material subroutine (UMAT) and called by the finite element package ABAQUS/Standard. More detailed description about the numerical implementation of the crystal plasticity constitutive model can be found elsewhere (Li and Huang, 2021). Given the limitation of the commercial finite element software in terms of mass diffusion, the hydrogen diffusion equilibrium equation needs to be solved using the heat analogy method (Abdolvand, 2019; Cui et al., 2021; Farukh et al., 2018).

The expression of Eq. (24) can be simplified as:

$$\frac{\partial C}{\partial t} + \nabla \cdot \mathbf{J} = 0 \quad (33)$$

Eq. (33) exhibits a strong resemblance to the equilibrium equation of heat transfer:

$$\rho \dot{U} + \nabla \cdot \mathbf{J}^q = 0 \quad (34)$$

As a consequence, the hydrogen diffusion equilibrium equation was incorporated into a user subroutine, UMATHT, which defines

Table 1
The implemented hydrogen diffusion equation.

	GI region	GB region
Hydrogen types	NILS-H D-H	GB-H D-H
Hydrogen flux	$\mathbf{J}_L = -D_g \mathbf{I} \cdot (\nabla C_L - \frac{C_L \bar{V}_H}{RT} \nabla \sigma_H)$	$J_k = -D_k \cdot (\nabla C_{GB-H} - \frac{C_{GB-H} \bar{V}_H}{RT} \nabla \sigma_H)$ $k = "GB, \perp": \mathbf{J} \text{ is vertical to the GB plane}$ $k = "GB, \parallel": \mathbf{J} \text{ is parallel to the GB plane}$
Diffusion coefficient	$D_g = D_{0g} \exp(-\frac{Q_B}{kT})$	$D_{GB,\perp} = D_{0g} \exp\left(-\frac{Q_B - Q_{seg}}{k_B T}\right)$ $D_{GB,\parallel} = \lambda D_{0g} \exp\left(-\frac{Q_B - \gamma_{GB}(\hat{a}/\hat{m})}{k_B T}\right)$
Equilibrium equation	$D_{eff} \frac{dC_\omega}{dt} + \theta_{TD}^\alpha \frac{dN_{TD}^\alpha}{d(\rho_{SSD}^\alpha + \rho_{GND}^\alpha)} \frac{d(\rho_{SSD}^\alpha + \rho_{GND}^\alpha)}{dt} + \nabla \cdot \mathbf{J}_\omega = 0$	

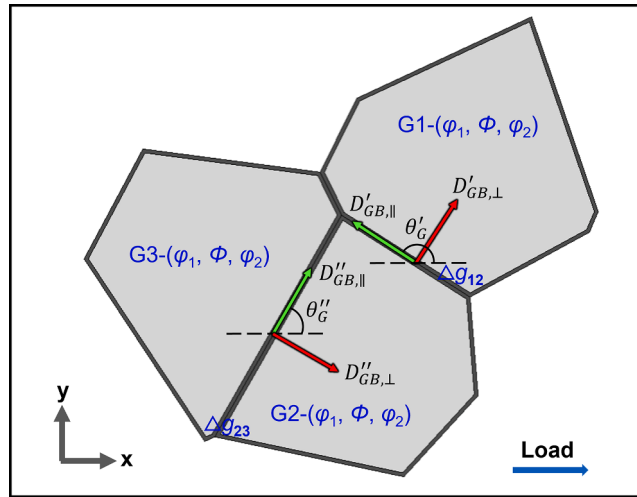


Fig. 2. Schematic diagram of the relationship between the diffusion tensor and GB characteristics.

the material's thermal behavior, by using equivalent alternative to the variables listed in [Table 2](#).

The calculation steps of HS gradient $\nabla\sigma_H$ in [Eq. \(23\)](#) are implemented using the global array within subroutine, and it is done in the UMATHT code. The calculation steps are as follows:

To ensure the existence of the HS gradient within the element, the three-dimensional quadratic element (C3D20RT) with reduced integration points is used in this work. The HS gradient can be expressed as:

$$\nabla\sigma_i = \partial\sigma_H / \partial X_i = \sum_{np=1}^8 (\partial N^{np} / \partial X_i) \sigma_H^{np} \quad (35)$$

where N^{np} is the shape function of C3D20RT element, X_i ($i = 1$ for x , $i = 2$ for y , $i = 3$ for z) refers to the global coordinates of the integration points in 3-dimensional space. However, N^{np} is a function of local coordinates, and the Jacobi matrix between local coordinates and global coordinates needs to be established to calculate $\partial N^{np} / \partial X_i$:

$$\partial N^{np} / \partial x_i = (\partial N^{np} / \partial X_j) \cdot (\partial X_j / \partial x_i) \quad (36)$$

where x_i ($i = 1$ for ξ , $i = 2$ for η , $i = 3$ for ζ) is referred to the local coordinate of the integration points. The Jacobi matrix J^{elt} can be expressed as:

$$J_{j,i}^{elt} = \partial X_j / \partial x_i = \sum_{np=1}^8 (\partial N^{np} / \partial x_i) \cdot X_j^{np} \quad (37)$$

The USDFLD subroutine calculates the HS by the updated stress provided by UMAT. And the updated HS and the global coordinates of each integration points are stored in the global arrays and then passed into UMATHT for the calculation of $\nabla\sigma_H$. The flow chart of numerical analysis is shown in [Fig. 3](#).

3. Computer models

Three models are built, i.e., single crystal, bicrystal, and polycrystal models, as shown in [Fig. 4](#). The six planes of all the models were named to be X0, X1, Y0, Y1, Z0, and Z1 according to the coordinate system, and the gray X0, Y0, Z0 symbols denote the back faces in each direction ([Fig. 4\(c\)](#)). The single crystal and polycrystalline models were used to calibrate the crystal plasticity parameters and hydrogen diffusion parameters. In addition, two types of boundaries conditions, i.e., external hydrogen and internal diffusion, were set

Table 2
Analogy between variables in heat transfer and diffusion.

Heat equation	Mass diffusion equation
$\dot{U}^q = c_p \dot{T}$	$\partial C / \partial t = \partial C_{total} / \partial t$
Degree of freedom: T	Degree of freedom: C_L / C_{GB-H}
Heat flux: \mathbf{J}^q	Hydrogen flux: \mathbf{J}_ω
Heat capacity: c_p	1
Density: ρ	1

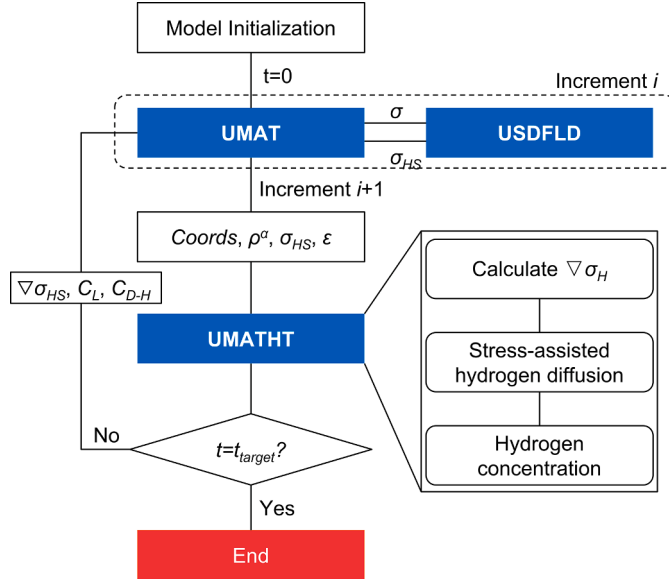


Fig. 3. Flow chart of numerical scheme for fully coupled analysis.

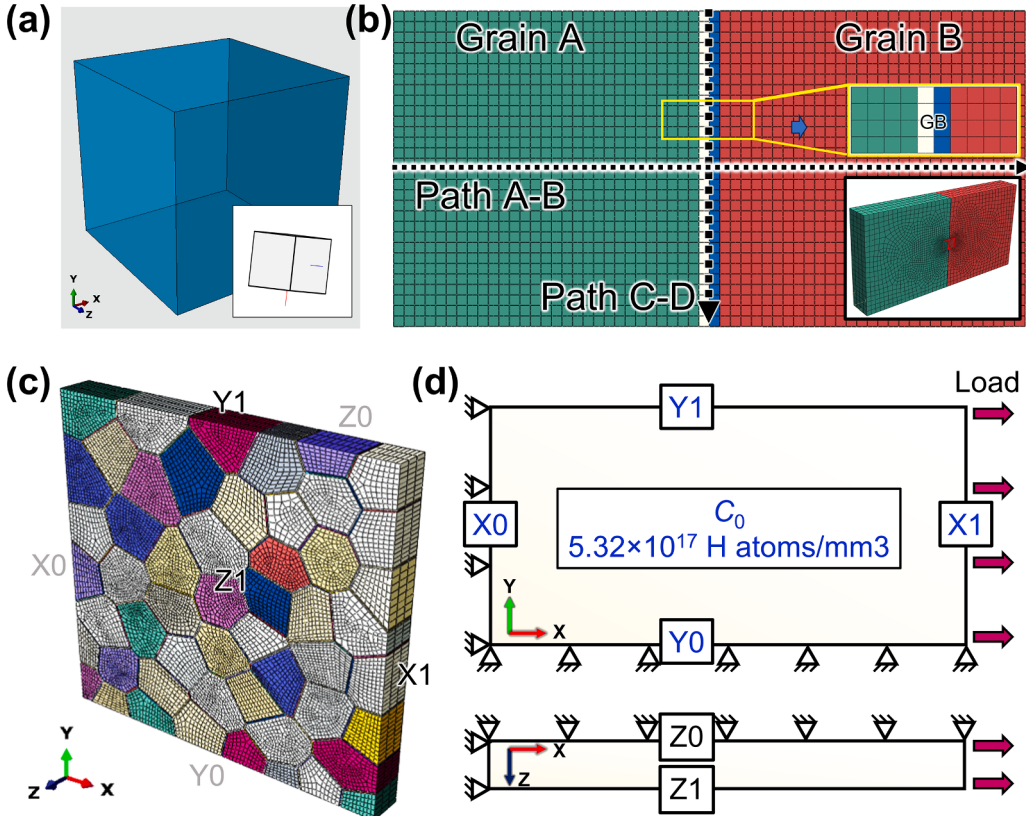


Fig. 4. Input models: (a) single crystal; (b) bicrystal; (c) polycrystal; (d) boundary conditions (internal hydrogen case).

up respectively in the bicrystal model to study the influence of GB characters on hydrogen diffusion. In order to avoid the boundary effects on the hydrogen concentration distribution, the central region of the bicrystal model was refined into smaller elements, with emphasis on the investigation of the hydrogen concentration distribution in this region (Fig. 4(b)). The quasi-3D polycrystal model was also used for analyzing the microstructure sensitivity of hydrogen diffusion in nickel. The [−1 6 7] axis of the single crystal was set to

be parallel to the x direction, i.e., the loading direction, to keep consistent with the experiment in literature (Yagodzinsky et al., 2008). And the orientation of the polycrystalline model was set to be random.

To investigate the hydrogen diffusion behavior at GBs, explicit GB layers with a constant thickness were incorporated into the bicrystal and polycrystal models in this study, and the GB layer consists of two elements through its thickness (Fig. 4(b)). In order to avoid the mesh sensitivity in the computational results, the thickness of GBs layer ranging from 1 μm to 5 μm was utilized to study the influence of GBs on material deformation (Biglari and Nikbin, 2015; Chandra et al., 2020; Zhao et al., 2017). Moreover, based on the calculation formula for GB layer thickness proposed in Fu et al. (2001), Zheng et al. (2022), it can be estimated that the thickness of GB layer falls approximately within the range of 0.667 μm to 2.057 μm when the averaged equivalent grain diameter ranges from 10 μm to 50 μm . Therefore, the thickness of GB layer in this work was set to be 1 μm .

In the simulations under the internal hydrogen condition, the nodes lying on X0, Y0, and Z0 planes of all the models (single crystal, bicrystal, and polycrystal models) were constrained along the x , y , and z directions, respectively (Fig. 4(d)). A constant positive loading velocity was set to the X1 plane, i.e., $9 \times 10^{-5} \text{ s}^{-1}$ for single crystal and $1 \times 10^{-5} \text{ s}^{-1}$ for the bicrystal and polycrystal model. In addition to the 2% tensile strain applied to the polycrystal model in the parameter identification part in Section 4.1, all other polycrystal models used for hydrogen diffusion simulations were subjected to a 1% strain, which is the same as the strain applied to the bicrystal and single crystal models, in order to facilitate comparison. The initial hydrogen concentration of all the nodes in the models were set to be $5.32 \times 10^{17} \text{ H atoms/mm}^3$ (100 wt. ppm). And a constant hydrogen concentration of $5.32 \times 10^{17} \text{ H atoms/mm}^3$ was assigned to all the nodes lying on the X0, X1, Y0, and Y1 planes, as shown in Fig. 4(d), in order to represent the interaction between the modelled grains with the rest of the material that is not modelled. All models were discretized into elements with an average size of 1.5 μm , except that the GB layers have an average size of 0.5 μm . The hydrogen transport behavior near the 26 STGBs listed in Table A1 and in the polycrystalline models with three grain sizes (19 μm , 16 μm , and 14 μm) shown in Fig. 5 were studied.

In the external hydrogen case, without applied load and only the plane X0 or Y1 is exposed to the hydrogen atmosphere with a concentration of $5.32 \times 10^{17} \text{ H atoms/mm}^3$ to simulate hydrogen atoms diffuse across or along GBs. And the hydrogen concentration of all the nodes in the models were set to be $10^{10} \text{ H atoms/mm}^3$ to avoid the oscillations caused by the initial steep concentration gradients (Sofronis and McMeeking, 1989).

4. Results and discussion

4.1. Model parameters and validation

The crystal plasticity model coupled with stress-assisted hydrogen diffusion presented in Section 2 is utilized to investigate the hydrogen transport behavior of the pure nickel during deformation, which depends on a number of physical parameters of the materials.

Nickel is a FCC material with a Zener anisotropic factor of $f = 2C_{44}/(C_{11} - C_{12}) = 2.44$ (Renner et al., 2016). The elastic constants are $C_{11}=249 \text{ GPa}$, $C_{12}=155 \text{ GPa}$, and $C_{44}=114 \text{ GPa}$ (Castelluccio and McDowell, 2017). The shear modulus can be calculated from the elastic constants. The interaction matrix $A^{\alpha\beta}$ in Eq. (4) is assumed to be governed by six coefficients (a_0-a_5) in the case of FCC crystal, which control the hardening process with different function (Franciosi et al., 1980; Keller et al., 2012), i.e., self-hardening (SH, a_0), coplanar (CP, a_1), Hirth-lock (HL, a_2), glissile junction (GJ, a_3), Lomer-Cottrell lock (LC, a_4) and cross-slip (CS, a_5). Values and arrangement of the six coefficients can be found in (Arsenlis and Parks, 2002). The length-interaction $H^{\alpha\alpha'}$ takes the same form as $A^{\alpha\beta}$ but with different values, as shown in Table 3. Gonzalez et al. (2014) found that the elastic constants of the GB elements have a minimal effect on the stress-strain response of the material, with the normal stresses at GB dominated by plastic anisotropy. According to the findings in Chandra et al. (2020), the Helmholtz free energy has a significant influence on materials deformation, while the influence of the remaining parameters of elements in GB region is negligible. Moreover, based on the conclusions from Liu and Sluiter (2023), GBs of nickel exhibit a low sensitivity to stress states. For the STGBs studied in our work, the incompatibility factor at GBs is close to zero based on the method proposed by Liu and Sluiter (2023), indicating a minor influence of elastic deformation. Consequently, in this study, the CPFE parameters of two-layer elements in the GB region remain consistent with their neighboring grains, except for the distinction in initial strength and hardening modulus.

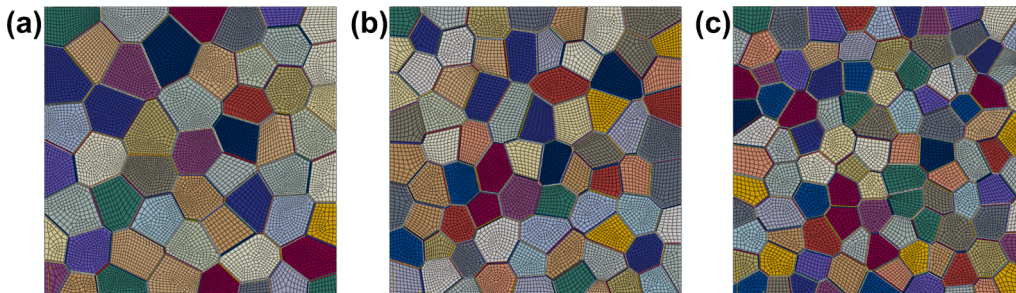


Fig. 5. Polycrystalline model with different grain size: (a) 19 μm ; (b) 16 μm ; (c) 14 μm .

Table 3

Coefficients of the dislocation interaction matrix (Keller et al., 2012).

Parameters	a_0	a_1	a_2	a_3	a_4	a_5
Magnitude	0.125	0.125	0.635	0.125	0.07	0.122
Parameters	h_0	h_1	h_2	h_3	h_4	h_5
Magnitude	0.0	0.038	0.38	0.27	0.02	1

In the hydrogen diffusion model, the binding energy of dislocation Q_{dis} and the concentration of the reversible traps sites N_{GB-H} , i.e. GBs are reported in literature (Lu et al., 2022a). The pre-exponential constant D_{0B} , GB activation energy Q_B and the value of \hat{a}^2 / \hat{m} are provided in the work of Page et al. (2021). All the parameters used in the hydrogen diffusion model is summarized in Table 4.

The tensile simulations were carried out on the single crystal and polycrystalline model with the strain rate of $9 \times 10^{-5} \text{ s}^{-1}$ and $1 \times 10^{-5} \text{ s}^{-1}$, respectively. And the experimental stress-strain curves of single crystal and polycrystal nickel were obtained from the literature (Arora et al., 2019; Yagodzinsky et al., 2008). From Fig. 6, it can be observed that the hydrogen diffusion constitutive model developed in this study, in conjunction with physically meaningful material parameters, is able to effectively capture the deformation behavior of both single crystal and polycrystalline nickel as well as the influence of hydrogen on deformation. The averaged strength of GB region g_{HP} was identified to be 27 MPa. And the parameters T_c and H_c in Eqs. (14) and (15) were calculated to be $1.2 \times 10^{-13} (\text{H atoms/mm}^3)^{-1}$. The crystal plasticity parameters used to model pure nickel are given in Table 5.

4.2. Bicrystal: external hydrogen case

The behavior of hydrogen diffusion across the STGBs was studied. The segregation energies of hydrogen atoms for STGBs in nickel were calculated via the embedded-atom method (Shiga et al., 2003). The results indicate that the segregation energies range between -0.36 eV and -0.26 eV , with an average value of -0.29 eV . And the GB energy of the [100]-STGBs reported in Page et al. (2021) is in the range between 0.771 J/m^2 and 1.360 J/m^2 . The effects of the segregation energy and GB energy on the trapping, detrapping, and diffusion of hydrogen atoms along GB were studied.

For the convenience of direct comparison, the hydrogen concentration is presented in logarithmic values in Fig. 7(a) and (c), whereas relative hydrogen concentration (C_m/C_0) is used for the rest of the results. The distributions of hydrogen concentration along path A-B and C-D are shown in Fig. 7. For a single crystal at constant temperature, the distribution of hydrogen concentration is dependent on both diffusion time and distance from the hydrogen source (Fig. 7(a) and (b)). The hydrogen trapping effect at GB is directly related to the magnitude of the segregation energy (Fig. 7(c)). For GB diffusion, the GB energy is the dominant factor that affects the hydrogen diffusivity. Simulation results confirm that GB serves as a fast pathway for hydrogen diffusion, and this acceleration effect is positively correlated with the magnitude of the GB energy (Fig. 7(d)).

Furthermore, we have observed that, for a short diffusion time or a small GB energy, the hydrogen concentration within GB firstly reaches a peak, as indicated by the region pointed by the gray arrowhead in the figure, and then decreases with increasing diffusion distance (Fig. 7(b) and (d)). This phenomenon is consistent with the diffusion behavior of Type-B and Type-C as described in (Harrison, 1961), both of which assume a constant thickness for GB. Type-B diffusion refers to the diffusion pattern in which the hydrogen concentration contour diagram forms “river-valleys”, as shown by the white dashed lines in Fig. 8. Combining with the results of this study, we can assume that this is caused by the different diffusivity of hydrogen along GB and inside the crystal, leading to the formation of the valleys. In order to maintain the hydrogen equilibrium between GI and GB, a hydrogen diffusion delay phenomenon occurs in GB, which is the source of the hydrogen concentration peak in Fig. 7(b) and (d). Subsequently, driven by the concentration gradient, this equilibrium state is disrupted and hydrogen atoms continue to diffuse towards the lower concentration direction. The mutual interaction between hydrogen diffusion in the two regions throughout the entire process jointly determines the distribution of hydrogen atoms inside the material. Fig. 8 shows that when the GB energy increases from 0.843 J/m^2 to 1.102 J/m^2 with the same diffusion time, the depth of the valley increases from $0.54 \mu\text{m}$ to $1.5 \mu\text{m}$. Additionally, the distance of hydrogen diffusion at GB is further than that at the top of the valley, which is also attributed to the effect of GB energy that promotes the hydrogen diffusion. This phenomenon is consistent with the Type-C diffusion in Harrison (1961). This is also why HE is primarily attributed to GBs, as even though the diffusion of hydrogen at GBs is constrained by the concentration of hydrogen within the grains, it does not impede the increase of hydrogen concentration at the far end of GB from the hydrogen source. And the concentrated hydrogen at the GB region is

Table 4

Hydrogen diffusion constitutive parameters.

Parameters	Magnitude	Units	Sources
N_L	9.134×10^{19}	sites/ mm^3	Calculated
N_{GB-H}	2.47×10^{20}	sites/ mm^3	(Lu et al., 2022b)
Q_{dis}	1.792×10^7	N-mm/mol	(Lu et al., 2022b)
D_{0B}	2.39×10^{-6}	m^2/s	(Page et al., 2021)
Q_B	0.458	eV	(Page et al., 2021)
k_B	8.617×10^{-5}	eV/K	Physical constant
\hat{m} / \hat{a}^2	0.49	\AA^{-2}	(Page et al., 2021)
λ	0.19	–	(Page et al., 2021)

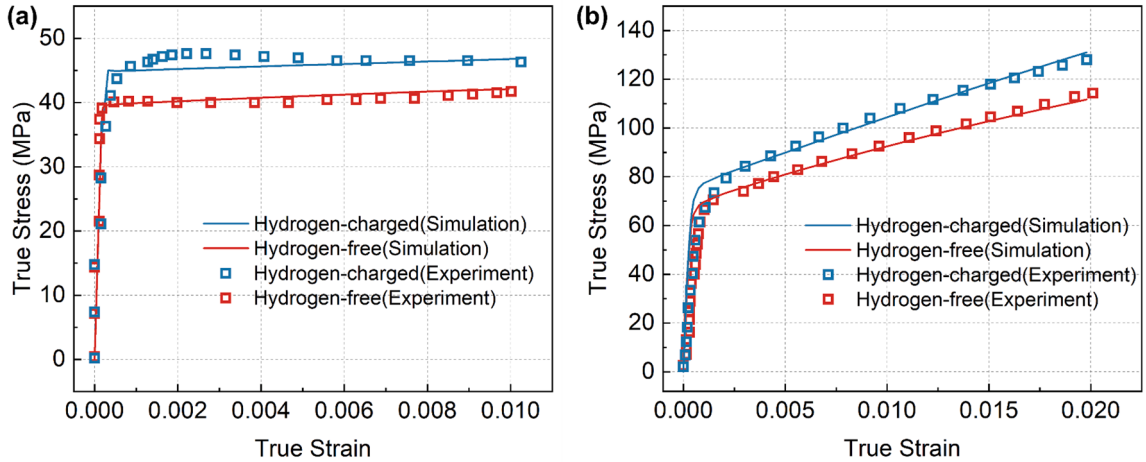


Fig. 6. Experimental and simulated stress-strain curves: (a) single crystal; (b) polycrystalline microstructure.

Table 5

Crystal plasticity constitutive model parameters.

Parameters	Magnitude	Units	Sources
b	0.25	nm	(Castelluccio and McDowell, 2017)
μ	58.4	GPa	Calculated
k_b	14	nm	Calculated
α_0	1	–	(Li and Huang, 2021)
ρ_0	1×10^6	mm ⁻³	Identified
n	15	–	Identified
$\dot{\gamma}_0$	1×10^{-3}	s ⁻¹	Identified
K	15/50	–	Polycrystalline/Single crystal - Identified

the culprit for crack initiation.

In addition, it is evident from Eqs. (19)–(21) that there exists a relationship between γ_{GB} and Q_{seg} . We further evaluated this relationship and found that it has a minimal influence on the simulation results during the diffusion process. The simulation pertaining to this aspect can be found in Appendix B.

4.3. Bicrystal: internal hydrogen case

The results in Appendix B demonstrate that the segregation energy has little effect on the hydrogen diffusion. Hence, the segregation energy remained as a constant of -0.26 eV in the subsequent simulations under internal hydrogen conditions. We investigated the hydrogen diffusion behavior near the [100]-STGBs mentioned in the literature (Page et al., 2021). The tilt angles range from 8.8° to 78.6° , and the STGBs and their energy are summarized in the Appendix C. Due to the symmetry of the STGBs, only the deformation and hydrogen concentration distribution on the left side of the STGBs were analyzed. The contour plots of the total relative hydrogen concentration and HS distribution along path A-B in 26 bicrystal models are shown in Fig. 9(a) and (b). The abscissa represents the normalized distance from GB, with 0 representing the GB region. Fig. 9(a) shows that the distribution of total hydrogen concentration is related to the distance from GB, with an enrichment of hydrogen concentration near GB. However, there are also several points in the far region from GB where hydrogen concentration is independent of the distance from GB. From Fig. 9(b), it is evident that there are significant HS within the material when the tilt angle is less than 30° . According to literature (Barrera et al., 2016; Díaz et al., 2016), hydrogen atoms tend to accumulate in regions with high HS. However, by comparing Fig. 9(a) and (b), it is apparent that the HS does not appear to be the direct cause of hydrogen accumulation.

We have examined the distribution of hydrogen concentration and HS along F1, F2, N1, and N2 paths shown in Fig. 9(a), as well as their correlation with the GB energy. The corresponding relationships are presented in Fig. 10. The GB energy is an inherent property of each GB, which does not change with the variation of the path. The distribution pattern of HS along the four paths is highly consistent. Specifically, at small tilt angles, the HS is relatively high, and it reaches a minimum value at around 65° tilt angle. The hydrogen concentration is highly sensitive to the path variation. It can be observed from Fig. 10 that the changes in hydrogen concentration along paths F1 and F2 are very similar to the variations in HS with respect to the tilt angle. Meanwhile, the hydrogen concentration along paths N1 and N2 is strongly correlated with the GB energy. Thus, the grain can be divided into two regions: near-GB region and far-GB region, as shown in Fig. 9(a). In the near-GB region, hydrogen concentration is highly correlated with the characteristics of GB, and hydrogen atoms tend to accumulate near GBs with high energy. On the other hand, the far-GB region is less affected by the GB

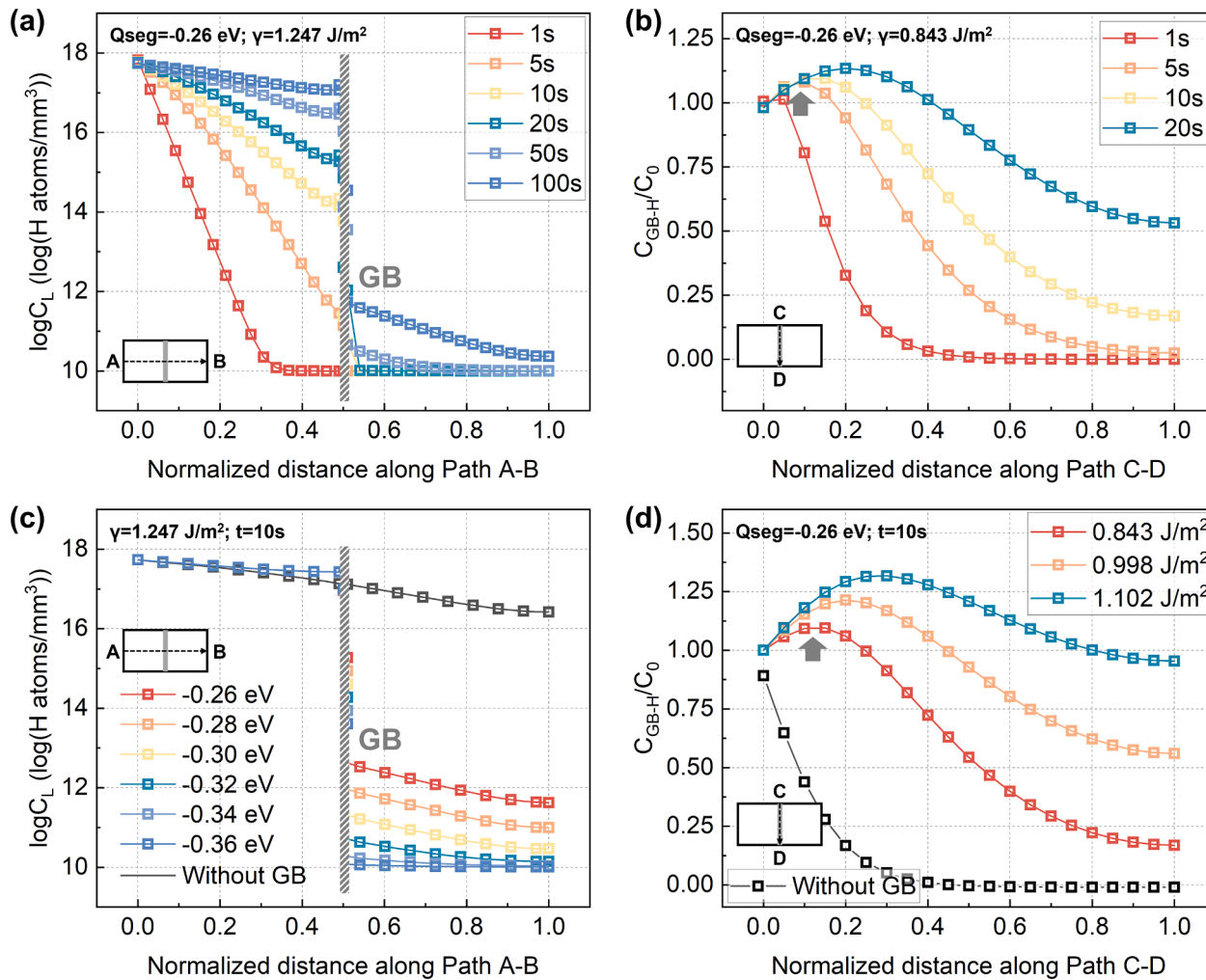


Fig. 7. The dependence of hydrogen concentration on the segregation energies and GB energies: (a) $\log C_L$ vs. diffusion time (crossing GB); (b) $C_{\text{GB-H}}/C_0$ vs. diffusion time (along GB); (c) $\log C_L$ vs. segregation energy; (d) $C_{\text{GB-H}}/C_0$ vs. GB energy.

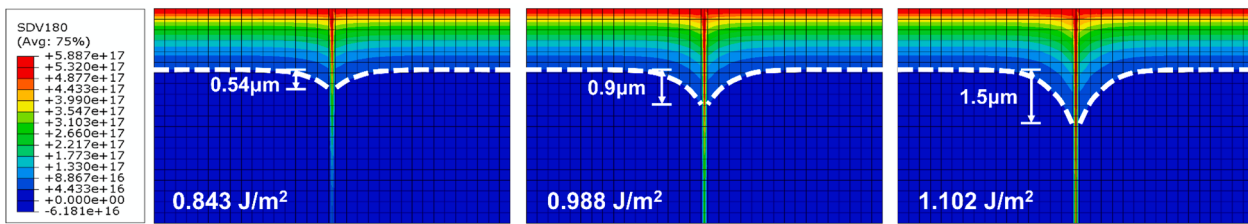


Fig. 8. C_{total} contour diagram forms “river-valleys” after 10 s in double-grain models with different GB energies.

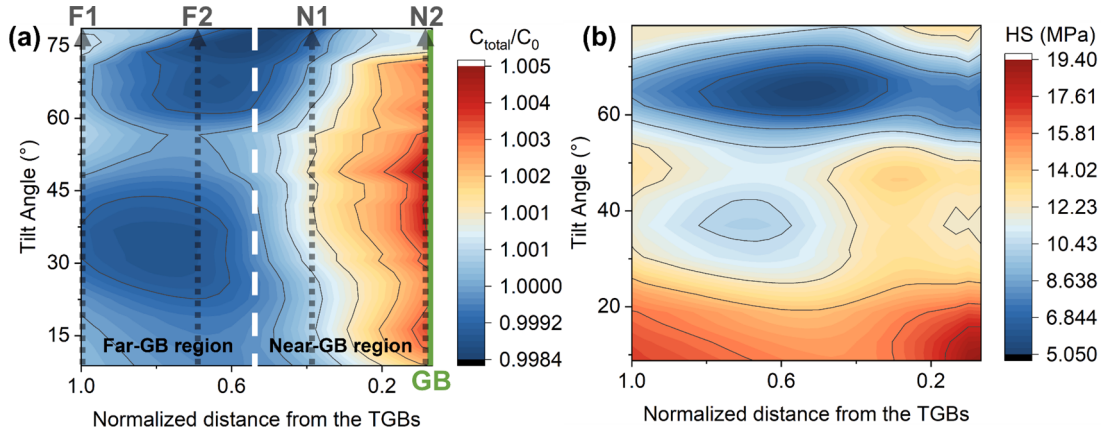


Fig. 9. Contour plots of the C_{total} (a) and HS (b) in the 26 bicrystal models.

energy, and hydrogen accumulation is mainly influenced by HS, with hydrogen atoms tending to accumulate in regions with higher HS. As described in Section 4.2, to maintain the continuity of concentration gradients within materials, fast diffusion in GBs is constrained by the diffusion in the grains nearby. From Fig. 8, it can be clearly seen that there is a difference in hydrogen concentration between the near-GB region and far-GB region, and the near-GB region with high GB energy has a larger size and higher hydrogen concentration. Therefore, high energy GBs are significantly favorable for H segregation and accumulation. This is also one of the main reasons why hydrogen embrittlement tends to initiate at HAGBs.

Dislocations have been confirmed to be another carrier for hydrogen transport (Chen et al., 2020; Yuan et al., 2022). The maximum dislocation density was calculated to be $9.86 \times 10^{-6} \text{ mm}^{-2}$ among 26 bicrystal models, and then the maximum number of dislocation trapping sites obtained by Eq. (18) was $3.983 \times 10^{13} \text{ sites/mm}^3$. Assuming the dislocation occupancy rate $\theta=100\%$, the maximum hydrogen concentration was calculated as $3.983 \times 10^{13} \text{ H atoms/mm}^3$, which was equal to the maximum number of trapping sites. The relationship between dislocation hydrogen and initial hydrogen concentration is given by the following equation:

$$\frac{C_{D-H}}{C_0} = \frac{\theta N_{D-H}}{C_0} \leq \frac{N_{D-H}}{C_0} \leq \frac{\max_{i=1}^{N_{\text{slip}}} (N_{D-H}^i)}{C_0} = \frac{3.983 \times 10^{13} \text{ Hatoms/mm}^3}{5.32 \times 10^{17} \text{ Hatoms/mm}^3} \approx 7.5 \times 10^{-5} \quad (38)$$

Compared to the total hydrogen concentration in Fig. 10, the ratio of C_{D-H} to the total hydrogen concentration is very small, and its effect on hydrogen accumulation is negligible. This is due to the small amount of dislocation multiplication caused by the small degree of plastic deformation (1%) used in this study, and the large initial hydrogen concentration further reduces the influence of D-H on the total hydrogen concentration. The sensitivity analysis of the mesh size and the thickness of GB layer for the current simulation results is presented in Appendix D.

4.4. Hydrogen transport in polycrystal

We conducted detailed studies on the hydrogen diffusion behavior in polycrystal, using a model with an average grain size of 19 μm . Fig. 11 shows the simulation results, where Fig. 11(a) represents the disorientation distribution map for each GB. It can be observed that the majority of GBs have a misorientation of 15° to 50° . The white GBs represent LAGBs ($<15^\circ$), which are highlighted by black dashed ellipses for easy viewing and description. Fig. 11(b) shows the distribution of HS, which exhibits strong microstructure sensitivity. Due to the severely heterogeneous deformation at GBs, they are the main locations of high HS, and in some grains, there are also large HS due to their specific orientations. Fig. 11(c) depicts the distribution map of the total hydrogen concentration inside the material. Under the influence of the HS and concentration gradient, hydrogen atoms tend to accumulate in some special regions, such as GB region and triple junctions. And also, the total hydrogen concentration in the GB region in Fig. 11(d) shows no significant enrichment within the LAGBs. The results further indicate that hydrogen does not tend to accumulate at LAGBs, even in the complex stress states of polycrystalline microstructure. Statistical analysis shows that the maximum hydrogen concentration at the dislocations is $3.608 \times 10^{15} \text{ H atoms/mm}^3$, which is only about 6.8×10^{-3} times the initial hydrogen concentration according to Eq. (38). However, the contribution of dislocation hydrogen to total hydrogen concentration cannot be ignored, as it is almost three orders of magnitude. This is due to the more complex shear deformation on the slip systems in polycrystal compared to the bicrystal model. In order to maintain local continuity, GNDs with higher densities occur at GBs, which reduces the MFP of SSDs and accelerates the multiplication of SSDs. Therefore, a large amount of hydrogen atoms trapped by dislocation cores are accumulated at GBs and near-GB region, while D-H concentration in the grains is relatively low.

Furthermore, taking into account practical service conditions where materials are typically subjected to prolonged loading, we have maintained the loading condition for an additional 105 s following the deformation studied in this section to explore the hydrogen diffusion within the polycrystalline materials under steady-state conditions. The results, as depicted in Fig. 12, demonstrate that with the extension of the loading duration, there is a reduction in the localized hydrogen concentration within the material due to

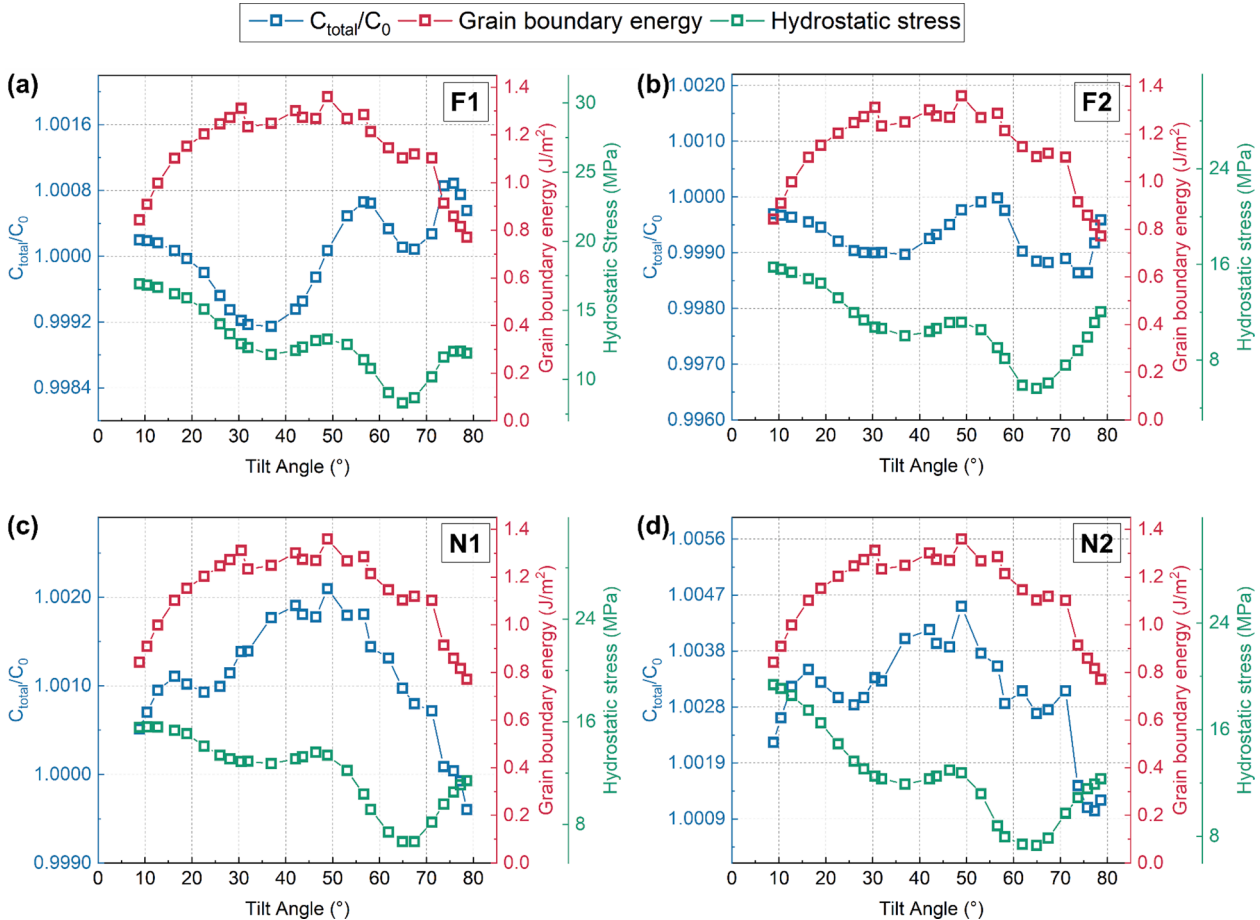


Fig. 10. The variation of GB energy, C_{total} and HS with respect to the tilt angle along the four paths: (a) F1; (b) F2; (c) N1; (d) N2.

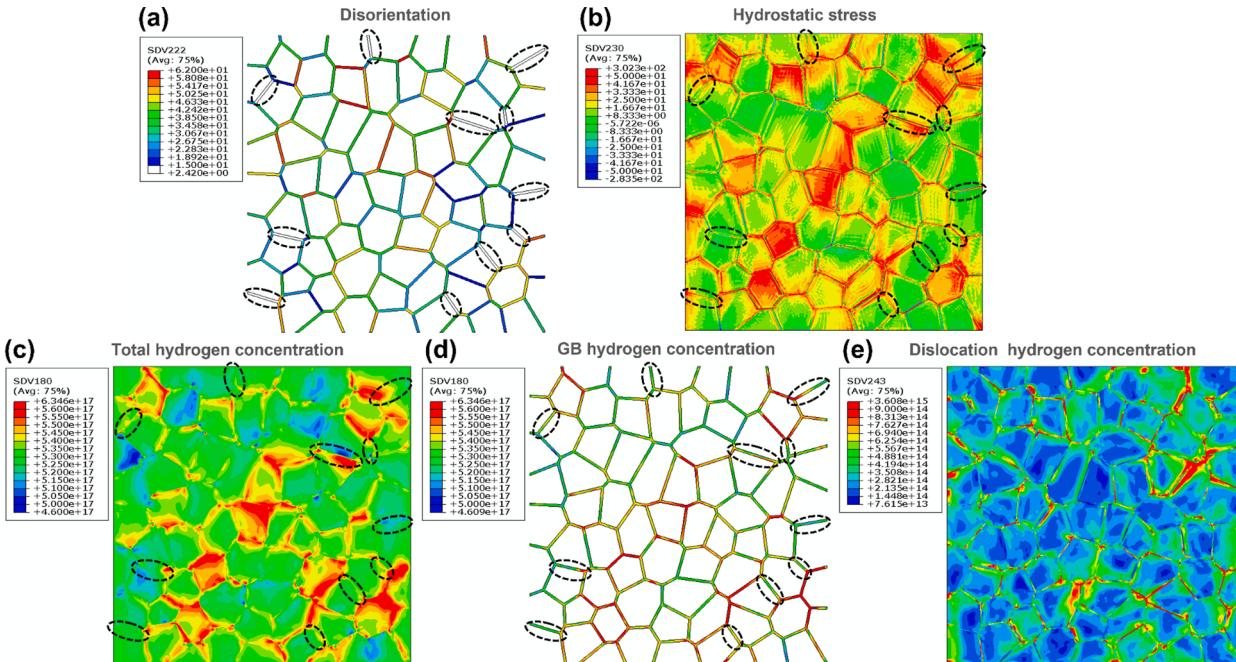


Fig. 11. Simulation results of the polycrystalline microstructure with an average size of 16 μm : (a) misorientation; (b) HS; (c) C_{total} ; (d) C_{total} in GB region; (e) $C_{\text{D-H}}$.

stress relaxation, given the utilization of a viscoplastic constitutive model in this study. However, the distribution is similar to the transient hydrogen concentration distribution. Fig. 13 illustrates the dependence of the average HS and hydrogen concentration within the material. Additionally, since the employed hydrogen diffusion model takes into account the dependence of hydrogen diffusion on HS gradient (Eq. (23)), a decrease in hydrogen concentration is observed. As the duration surpasses 2×10^4 s, both the HS and hydrogen concentration within the material reach a stable range, entering a steady-state diffusion.

In addition, a comparative simulation was performed by excluding the effect of GB energy on hydrogen diffusion. Further analysis and discussion were conducted on factors such as hydrogen concentration and HS for various grain combinations enclosed by the black dashed line in Fig. 12(d) under steady-state conditions. Regarding combination #1, as depicted in Fig. 14(a) and (b), under steady-state conditions, hydrogen continues to exhibit a propensity for distribution in the near-GB regions, as well as in areas of high HS within GI regions. When the effect of GB energy is not considered (Fig. 14(e) and (f)), hydrogen primarily accumulates in regions characterized by high HS. And from Fig. 14(c), (d), (g) and (h), it is apparent that the presence of GB energy leads to higher HS gradients in GB regions compared to scenarios where GB energies are not considered. This phenomenon is one of the crucial factors contributing to the enrichment of hydrogen near GB. The simulation results for combination #2 and #3 exhibit similar trends to #1 and are provided in Appendix E. The variations in hydrogen concentration and HS along paths P1 and P2 were also extracted and illustrated in Fig. 15. The results for both paths indicate that the regions with high HS correspond to elevated hydrogen concentrations. The presence of GB exacerbates the localized hydrogen concentration near GBs, while also leading to distinct HS jumps in their vicinity. This observation underscores the crucial role of GBs in the process of hydrogen diffusion, consistent with the conclusions drawn in Section 4.3. Moreover, it underscores the advantages of the methodology employed in this study for investigating the hydrogen diffusion in polycrystalline materials.

Based on the current model, we further investigated the hydrogen transport behavior in models with different grain sizes, i.e., different volume fractions of GBs, providing a theoretical basis for understanding the relationship between grain size and hydrogen embrittlement. The distribution of relative hydrogen concentration in the GI region and GB region for different microstructure were statistically analyzed, as shown in Fig. 16. Fig. 16(a) reveals that the hydrogen is more concentrated inside the grains compared to that at GBs, and the hydrogen concentration strictly follows a Gaussian distribution. The expectation and variance of the hydrogen concentration distribution in each model were calculated, as shown in Fig. 16(b). Increasing the grain size results in a higher relative hydrogen concentration inside the grains and a decrease in variance, while the hydrogen concentration at GBs decreases with an

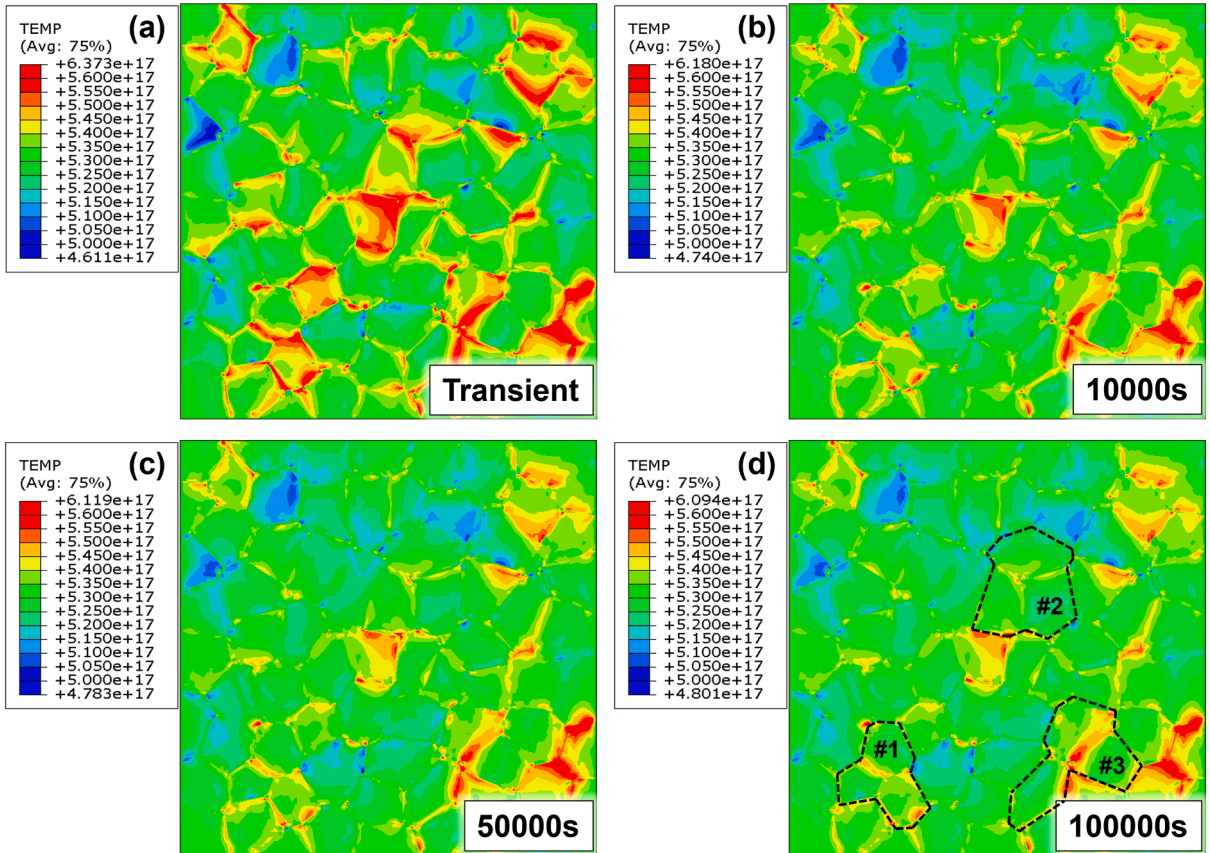


Fig. 12. Contour plots of hydrogen concentration at different time intervals: (a) transient; (b) 10000s; (c) 50,000 s; (d) 100000s.

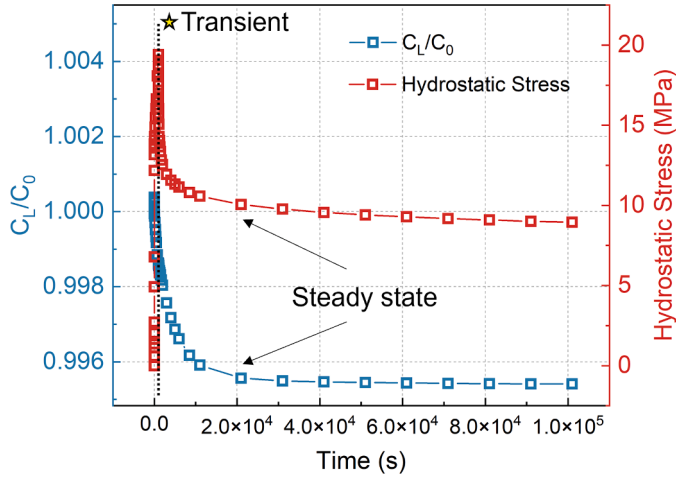


Fig. 13. Evolution of relative hydrogen concentration and HS over the time.

increase of variance. As discussed in [Section 4.3](#), hydrogen atom generally diffuses and accumulates near GBs under the influence of HS and concentration gradients. Therefore, a decrease in grain size leads to an increase in the volume fraction of GBs within the material, resulting in a higher concentration of hydrogen in these regions. Since there is no external source of hydrogen under internal hydrogen case, the hydrogen concentration inside the material follows the law of mass conservation. Thus, the hydrogen concentration inside the grains decreases with an increase in grain size. The value of the hydrogen concentration distribution variance represents the uniformity of hydrogen distribution, and higher variance indicates more heterogeneous distribution. As the grain size decreases, the increase in the volume fraction of the near-GB region exacerbates the heterogeneity of hydrogen concentration within the grains. On the other hand, the hydrogen concentration inside GB is strongly related to the GB energy. As the number of GB increases, the discreteness of the interfacial energies decreases, resulting in a more homogeneous distribution of hydrogen within GB. Therefore, both excessively large and small grain sizes can degrade the HE resistance of a material. In microstructures with intermediate grain sizes, hydrogen concentration at GBs is more evenly distributed with a lower magnitude, which has significant implications in the design of HE-resistant alloys through microstructure control.

4.5. Exploration and analysis of the mechanism of hydrogen-assisted cracking mechanisms

This study indicates that the diffusion and distribution of hydrogen atoms within the material are highly sensitive to the characteristics of GBs, which may be one of the key reasons for the transition from ductile to brittle fracture. Therefore, the model described in [Section 2](#) of this study was also integrated with the phase-field model to predict the process of hydrogen-assisted cracking. The setup of boundary conditions and the numerical solution process are presented in [Appendix F](#).

[Fig. 17](#) and [Fig. 18](#) illustrate the distribution of crack and hydrogen concentration under external hydrogen condition at different time, respectively. In [Fig. 17](#), the red arrows indicate the position of the primary crack tip, while the blue arrows represent the position of the secondary crack. To facilitate the assessment of the crack propagation path, the trajectories of GBs are added in [Fig. 17\(f\)](#). From the figure, it can be observed that the crack propagates along GBs, and there are secondary cracks present near the primary crack tip. Subsequently, during deformation, the primary crack merges with the secondary crack, forming an updated primary crack. Comparing with [Fig. F.1\(b\)](#), it is evident that the crack primarily extends along the HAGBs. [Fig. 18](#) demonstrates that a high concentration of hydrogen is observed at the tip of the secondary crack, which promotes the propagation of the secondary crack and its merging with the primary crack.

[Fig. 19](#) and [Fig. 20](#) represent the crack and hydrogen concentration distribution, respectively, during the cracking propagation process under internal hydrogen conditions. The red and blue arrows have the same indications as in [Figs. 17](#) and [18](#). From [Fig. 19](#), it can be observed that crack propagation still exhibits the phenomenon of primary and secondary crack merging. Additionally, [Fig. 20](#) reveals the presence of high hydrogen concentration at the tip of the secondary crack. The main difference between internal and external hydrogen conditions is that under internal hydrogen conditions, the hydrogen concentration at the crack tip is higher, while the rest of the material exhibits a relatively uniform hydrogen concentration. On the other hand, under external hydrogen conditions ([Fig. 18](#)), apart from the high hydrogen concentration at the crack tip, the hydrogen concentration is also elevated near the left boundary and the crack surface due to the influence of the external hydrogen source.

Based on the detailed analysis of the above results and in conjunction with the HEDE mechanism, the sequence of hydrogen-assisted crack propagation can be proposed, with schematic illustrations shown in [Figs. 21](#) and [22](#). In the figures, the blue and black line segments represent random HAGBs and LAGBs, respectively. The red particles represent hydrogen atoms, and the green line represents the crack surface.

In the external hydrogen case, i.e., the material is exposed to a hydrogen atmosphere and subjected to an external loading:

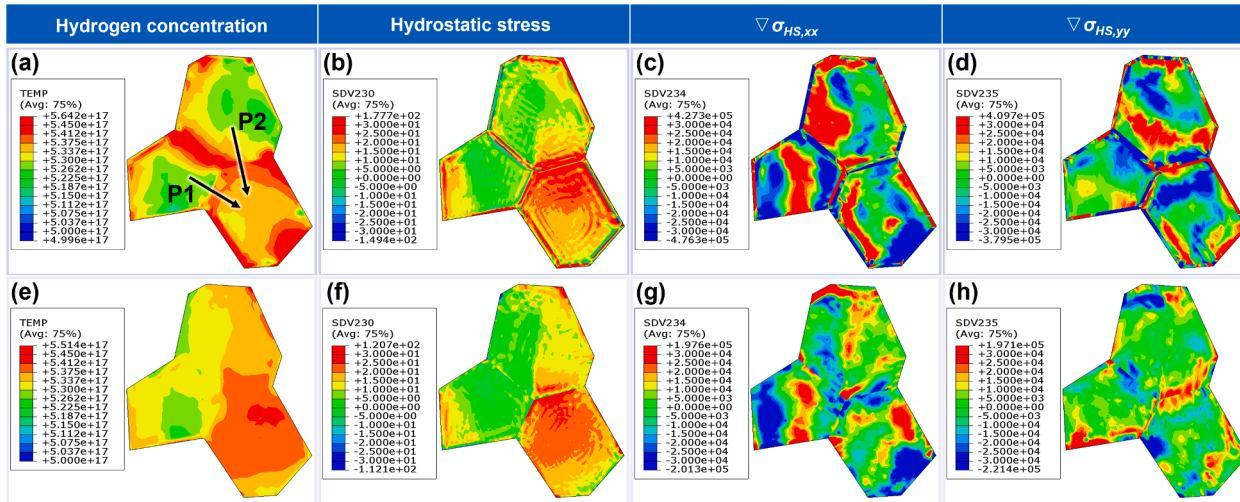


Fig. 14. Contour plots of hydrogen concentration, HS and its gradient for grain combination #1: (a)–(d): with GB energy; (e), (f): without GB energy.

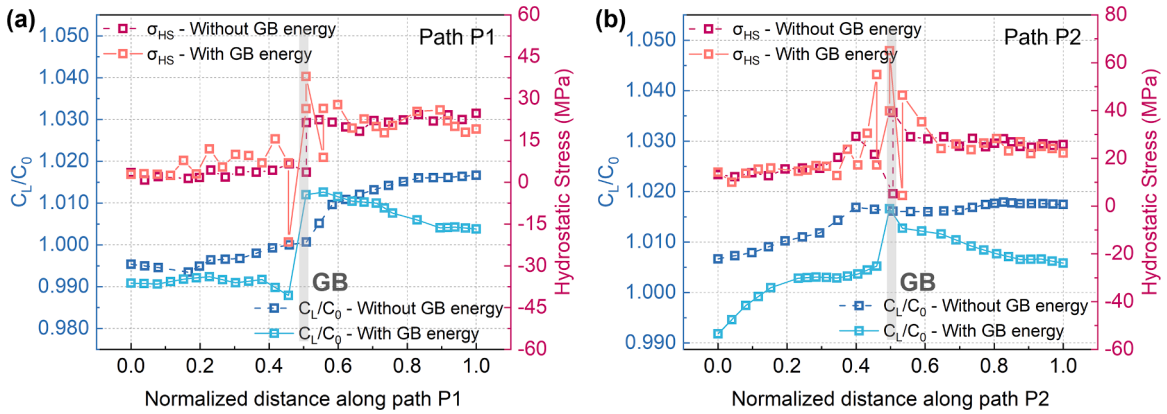


Fig. 15. Distribution of hydrogen concentration and HS along paths perpendicular to GBs: (a) path P1; (b) path P2.

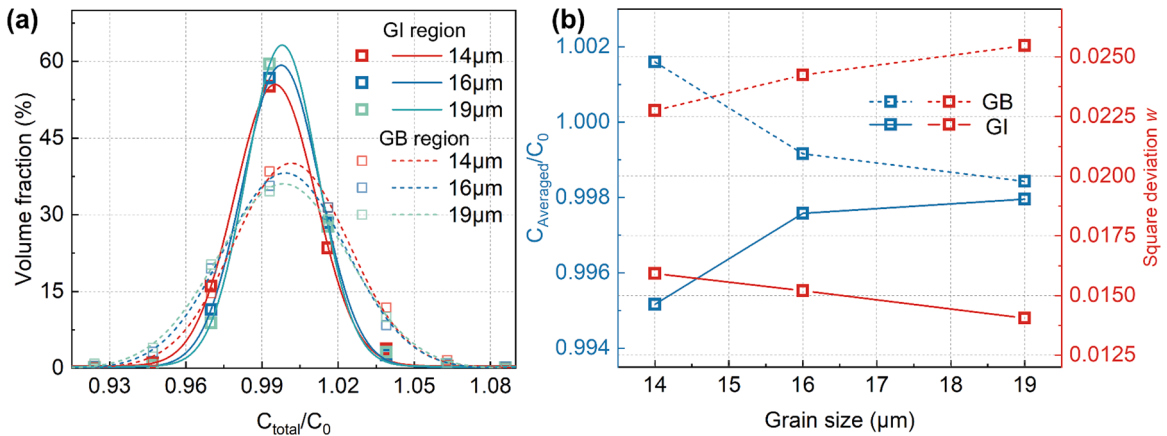


Fig. 16. The hydrogen concentration distribution considering the polycrystalline microstructure (a), and the dependence of expectation and variance on the grain size (b).

Step I: Hydrogen atoms first diffuse rapidly along the grain boundaries and simultaneously drives hydrogen atoms in the near-GB region to diffuse towards low concentration regions, as shown in Fig. 21(a).

Step II: As the diffusion process proceeds, the high concentration of hydrogen atoms at the far end of GB region weakens the cohesive strength of GB due to the Type-C diffusion mentioned in Section 4.2, which, together with the external load, causes decohesion of GB, leading to the initiation of cracks (Fig. 21(b)).

Step III: After the crack formation, the external hydrogen diffuses into GB at the crack front from the surface of the crack tip. A HS field appears near the crack tip, which is much higher than that inside the grains, promoting the accumulation of hydrogen atoms. Meanwhile, dislocations emitting from the crack tip may carry some hydrogen atoms away, but this does not affect the significant accumulation of hydrogen atoms at the crack tip. This will further promote the weakening of GB cohesive strength and induce the decohesion of GB, leading to the initiation of secondary cracks in front of the crack (Fig. 21(c)).

Step IV: The merging of the main and secondary cracks promotes the propagation of the crack, and new secondary cracks will appear again at the front of the new crack (Fig. 21(d)).

In the internal hydrogen case:

Step I: Stress promotes the concentration of hydrogen atoms in the vicinity of random HAGBs in H-charged materials, as well as the HAGBs themselves, due to their typically higher GB energies and the high density of GNDs (Fig. 22(a)).

Step II: When the hydrogen concentration at certain locations reaches the critical value, the cohesive strength of GB is weakened, resulting in successive GB decohesion process (Fig. 22(b)).

Step III: The crack initiated at the first debonded location is called the primary crack, while the small cracks that appear at other locations are referred to secondary cracks. The tip of primary crack generates a significant HS field, intensifying the accumulation of hydrogen atoms, accelerating GB decohesion in the vicinity of the secondary cracks (Fig. 22(c)).

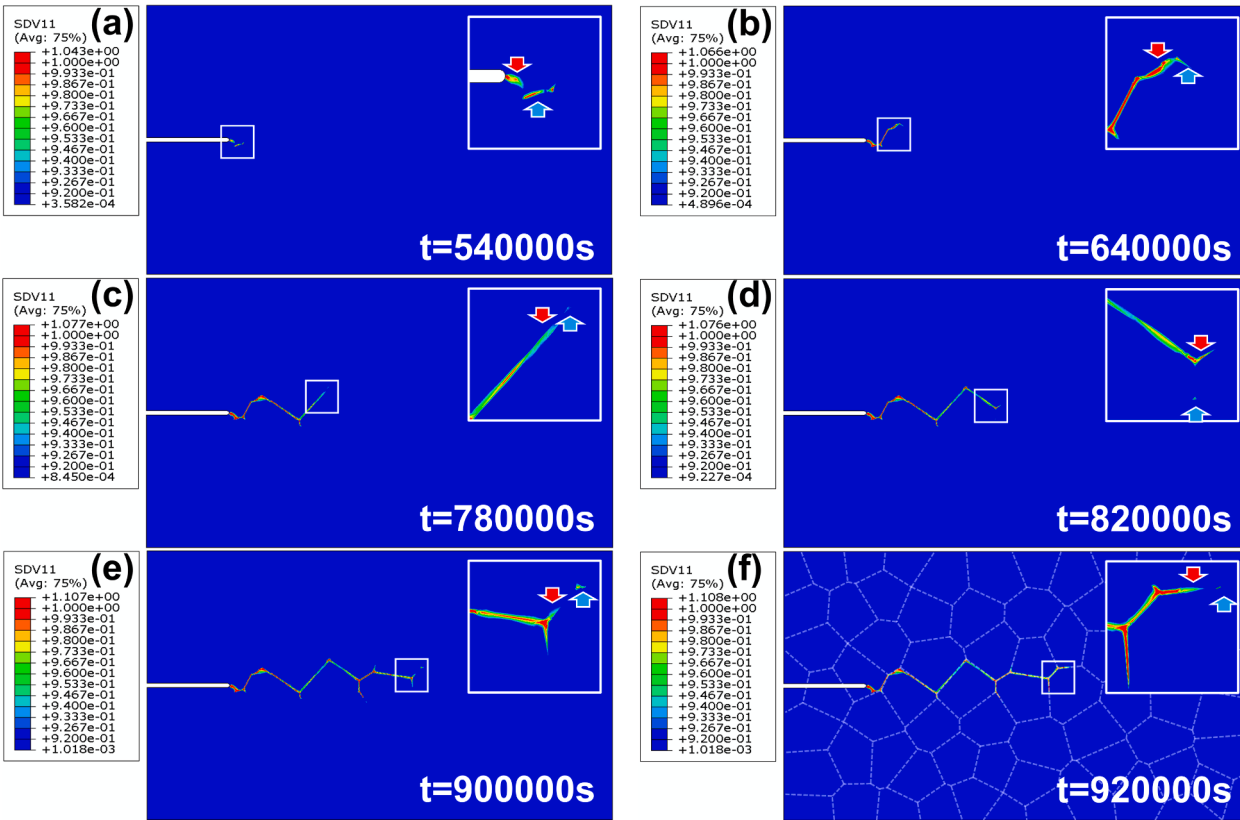


Fig. 17. Crack propagation diagram under external hydrogen conditions: (a) $t = 540,000$ s; (b) $t = 640,000$ s; (c) $t = 780,000$ s; (d) $t = 820,000$ s; (e) $t = 900,000$ s; (f) $t = 920,000$ s.

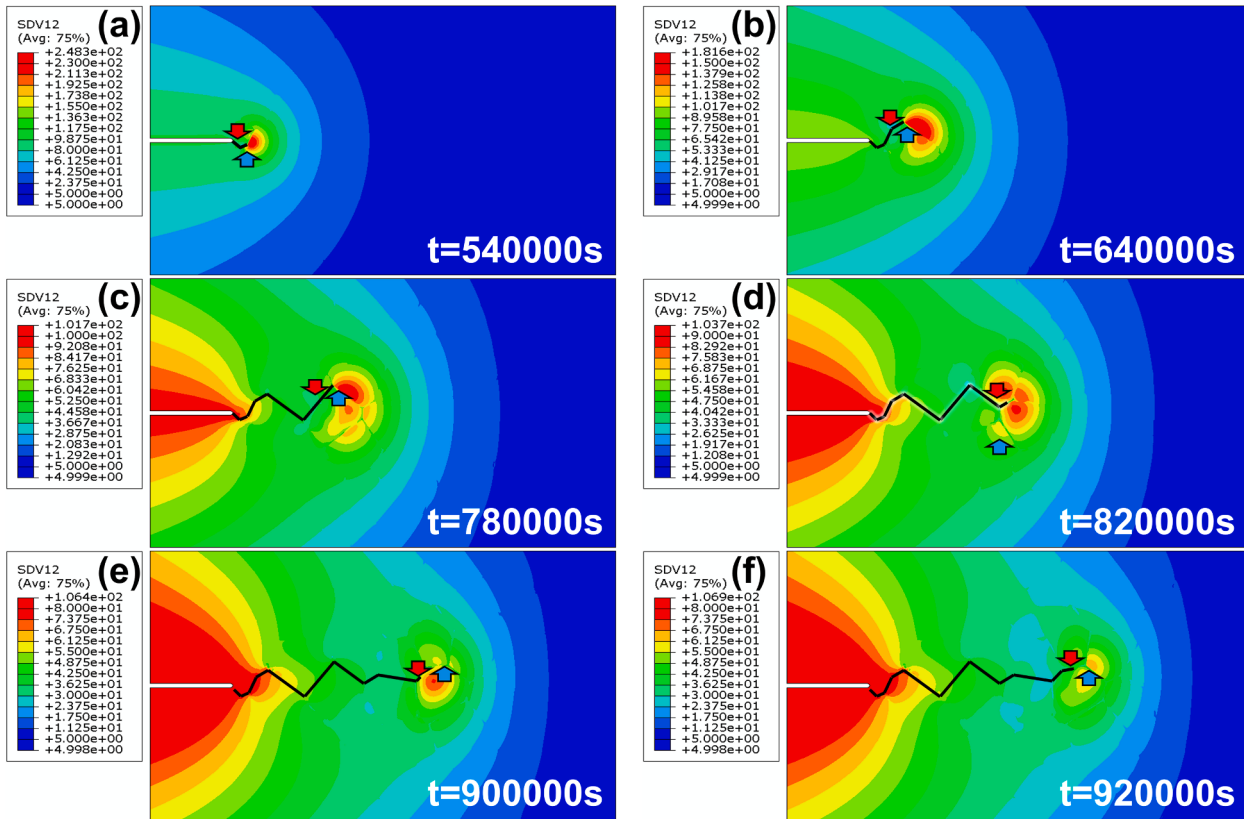


Fig. 18. The distribution diagram of hydrogen concentration during crack propagation under external hydrogen conditions with crack path denoted by black lines: (a) $t = 540,000$ s; (b) $t = 640,000$ s; (c) $t = 780,000$ s; (d) $t = 820,000$ s; (e) $t = 900,000$ s; (f) $t = 920,000$ s.

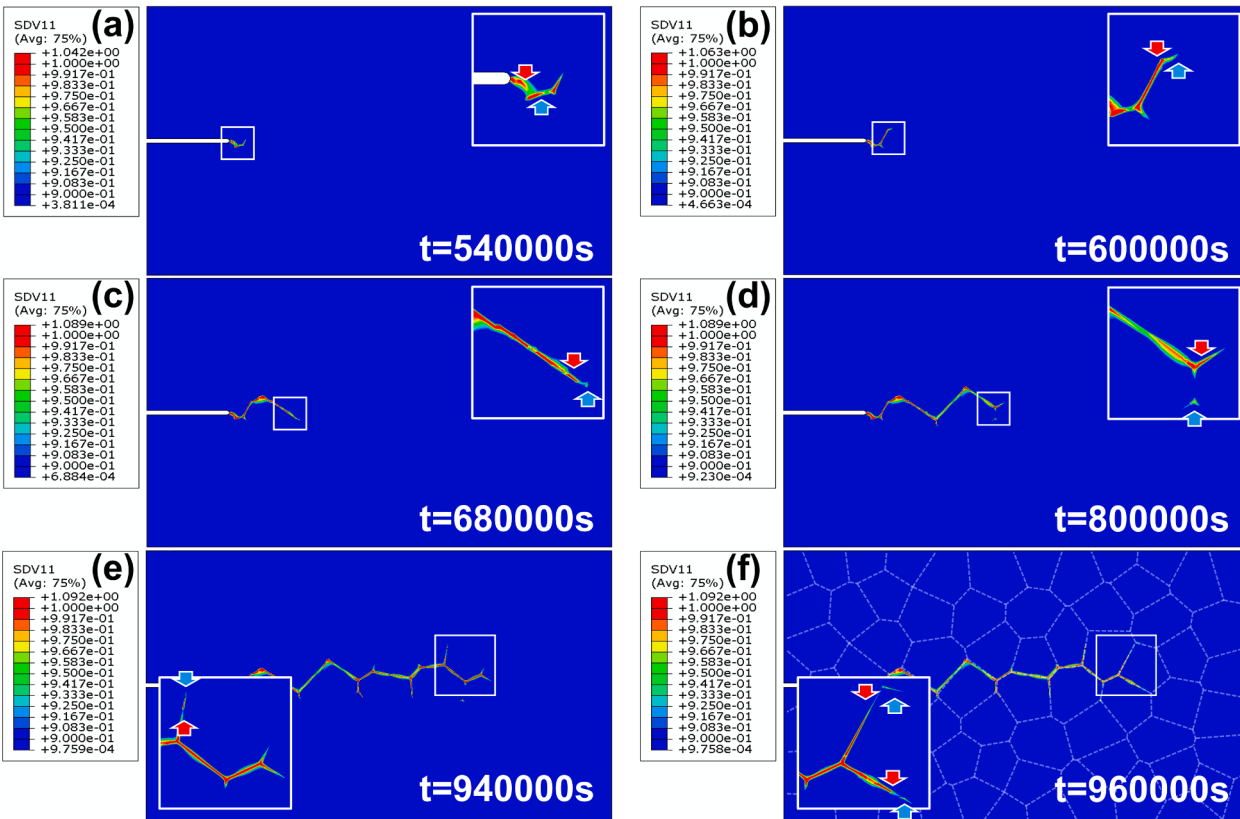


Fig. 19. Crack propagation diagram under internal hydrogen conditions: (a) $t = 540,000\text{ s}$; (b) $t = 600,000\text{ s}$; (c) $t = 680,000\text{ s}$; (d) $t = 800,000\text{ s}$; (e) $t = 940,000\text{ s}$; (f) $t = 960,000\text{ s}$.

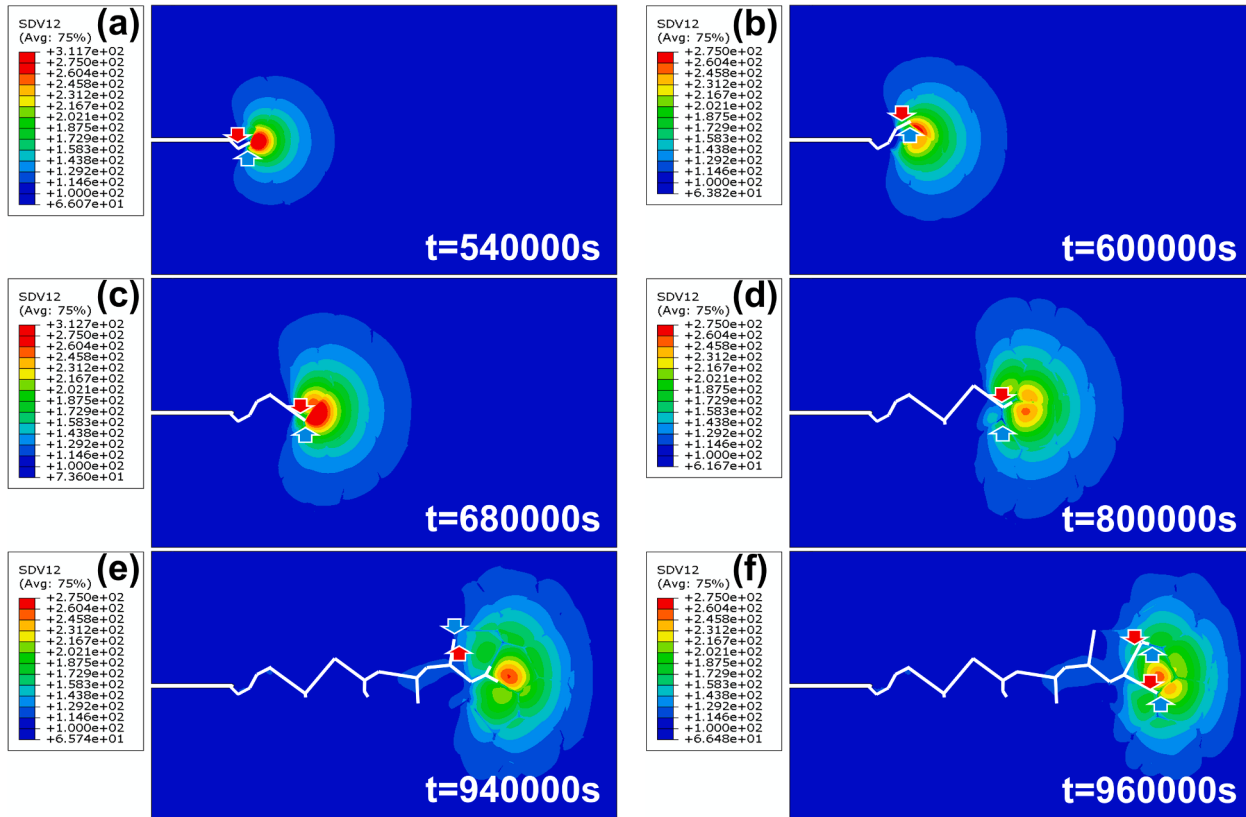


Fig. 20. The distribution diagram of hydrogen concentration during crack propagation under external hydrogen conditions, with crack path denoted by white lines: (a) $t = 540,000\text{ s}$; (b) $t = 600,000\text{ s}$; (c) $t = 680,000\text{ s}$; (d) $t = 800,000\text{ s}$; (e) $t = 940,000\text{ s}$; (f) $t = 960,000\text{ s}$.

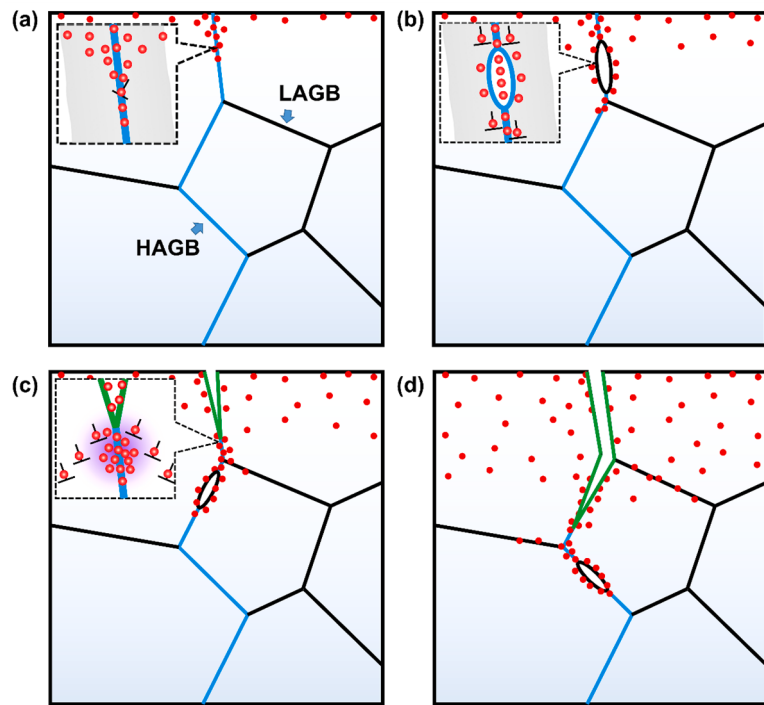


Fig. 21. Schematic diagram of the mechanism of hydrogen-assisted cracking under external hydrogen conditions: (a) step I; (b) step II; (c) step III; (d) step IV.

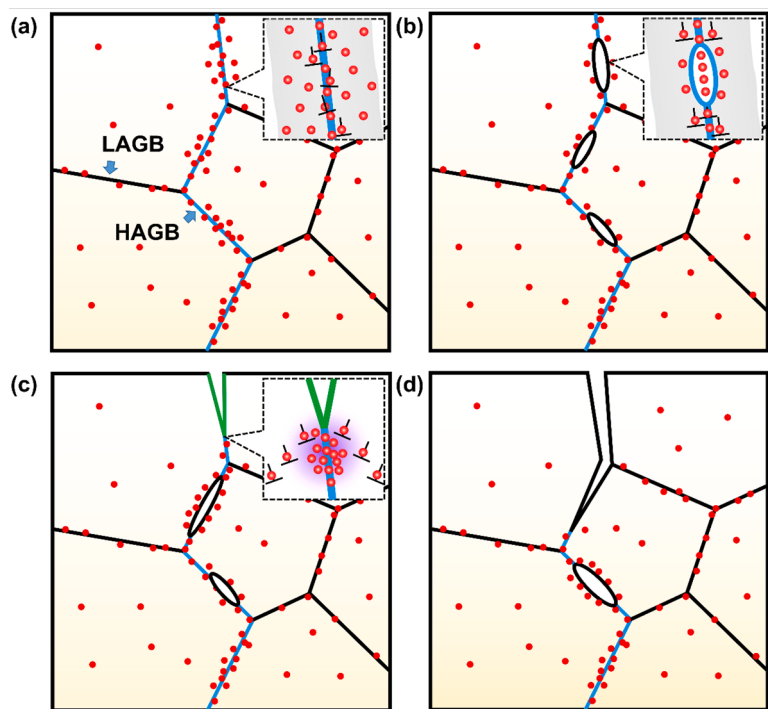


Fig. 22. Schematic diagram of the mechanism of hydrogen-assisted cracking in H-charged material: (a) step I; (b) step II; (c) step III; (d) step IV.

Step IV: When the ligament between the primary crack and the secondary cracks completely separates, they merge into a new primary crack, which continues to expand rapidly by merging with other secondary cracks in the same manner during deformation.

In summary, the crack propagation under either internal or external hydrogen conditions involves the gradual merging of the primary and secondary cracks, which is consistent with the findings in Ogawa et al. (2020). The results also demonstrate the accuracy of the model established in this study for predicting the hydrogen concentration distribution in the polycrystal materials, and confirm the feasibility of utilizing the phase-field method to predict the service life of materials in hydrogen environments.

5. Conclusion

In this study, a novel hydrogen diffusion model was coupled with the CPFE framework, taking into account the effects of GB characteristics on hydrogen diffusion. Subsequently, the hydrogen-assisted cracking phenomenon was further predicted. The key findings are as follows:

- (1) The polycrystal and bicrystal models were divided into GI and GB regions. The effect of hydrogen on the material's yield strength and hardening modulus was considered in the CPFE model, and the GB properties were considered in the hydrogen diffusion constitutive model. The coupled model was used to investigate the trapping, detrappling, and acceleration effects of GBs on hydrogen transportation.
- (2) The GB regions serve as a fast pathway for hydrogen diffusion; however, when GB-H attempts to escape from GB trapping sites, it is constrained by the GB segregation energy.
- (3) The transportation of hydrogen along GB is impeded by the hydrogen concentration in the near-GB region, resulting in the accumulation of a large number of hydrogen atoms at the peak of "river-valleys". The increase of GB energy exacerbates this phenomenon.
- (4) The hydrogen concentration in the near-GB region is dominated by the GB energy, while in the far-GB region, it is governed by HS. Additionally, simulation results indicate that hydrogen atoms tend to accumulate at HAGBs and triple junctions. Under steady-state diffusion conditions, the pattern of hydrogen distribution remains almost unchanged, but with a reduction in concentration attributed to the influence of HS.
- (5) For polycrystal model, those with moderate grain size exhibit better hydrogen tolerance, with low average hydrogen concentration and more uniform distribution.
- (6) Regardless of whether the material is in a hydrogen environment or pre-charged with hydrogen, the crack propagation is caused by the coalescence of primary and secondary cracks. The secondary cracks primarily initiate at HAGBs and triple junctions.

To sum up, the modified model shows a good capability in describing the fluctuations in mechanical properties of materials induced by hydrogen, and can predict hydrogen diffusion behavior in single-crystal to polycrystalline models under various hydrogen conditions, especially the influence of microstructure on hydrogen diffusion. This model can assist with the optimization of microstructure in HE-resistant alloys. And furthermore, it can be used to predict the crack growth rate and service life of materials by combining with phase-field model.

CRediT authorship contribution statement

Kaidi Li: Conceptualization, Methodology, Investigation, Software, Writing – original draft. **Bin Tang:** Supervision, Methodology, Writing – review & editing. **Mengqi Zhang:** Conceptualization, Resources. **Liguo Zhao:** Supervision, Methodology, Software, Writing – review & editing. **Xudong Liu:** Investigation, Formal analysis. **Jiangkun Fan:** Resources, Funding acquisition. **Jinshan Li:** Supervision, Funding acquisition, Writing – review & editing.

Declaration of Competing Interest

The authors declare that they have no known competing financial interests or personal relationships that could have appeared to influence the work reported in this paper.

Data availability

Data will be made available on request.

Acknowledgement

The authors would like to gratefully acknowledge the funding support from National Science and Technology Major Project of China (Grant No. J2019-VI-0023-0140) and the National Key Research and Development Program of China (No. 2021YFB3702604).

Appendix A. Analysis about the strength of the GB region

The strength of GB region reflects its hindrance effect on dislocation slip, resulting in localized and concentrated stress fields. Research shows that the hindrance effect is correlated with the GB energy. The GB energy influences the possibility of dislocation transmission. The high energy barrier impedes dislocation motion and results in GB strengthening (Huang et al., 2022). Therefore, it can be understood that high-energy GBs generally have higher strength of the GB layer compared to low-energy GBs. To assess the impact of g_{HP} on the simulation results, we take the example of the $\Sigma 29a$ (250) STGB and adjust the strength of its GB layer. As shown in Fig. A.1, the GB strength has the most significant influence on the hydrogen concentration in the near-GB region and the HS in the far-GB region. Under three different GB strengths, the maximum errors in the relative hydrogen concentration and HS are 0.161% and 8.689%, respectively, calculated using the following equations:

$$\text{Error} = \frac{\max_i\{\zeta_i\} - \min_i\{\zeta_i\}}{\bar{\zeta}} \times 100i = \{22, 27, 32\} \quad (\text{A.1})$$

where ζ_i represents either hydrogen concentration or HS, while the index i denotes the corresponding data for each g_{HP} . $\bar{\zeta}$ is the reference data, specifically representing the hydrogen concentration or HS when the GB strength is 27 MPa. This choice is based on the fact that the simulations in this paper are carried out using a GB strength of 27 MPa. When calculating the errors using the same method later on, the data used in the simulations mentioned in the main text is likewise chosen as the reference value.

From Fig. A.1, it can also be observed that the HS in the far-GB region decreases with increasing GB strength, leading to a reduction in hydrogen concentration in that region. In contrast, at the near-GB region, the increase in the GB strength does not affect the HS but results in an increase in hydrogen concentration. The research in Section 4.3 demonstrates that the hydrogen concentration in near-GB region is dominated by the GB energy. As mentioned earlier, high-energy GBs typically lead to a high strength of GB layer, which further enhances the GB energy sensitivity of the hydrogen concentration in the near-GB region.

Therefore, it is feasible to use the averaged GB strength, refers to g_{HP} , to describe the obtained trend of hydrogen transportation in the materials. The use of averaged strength somewhat weakens the conclusions stated in Section 4.3. However, the maximum error in hydrogen concentration is within 1%, which further demonstrates the accuracy of the results.

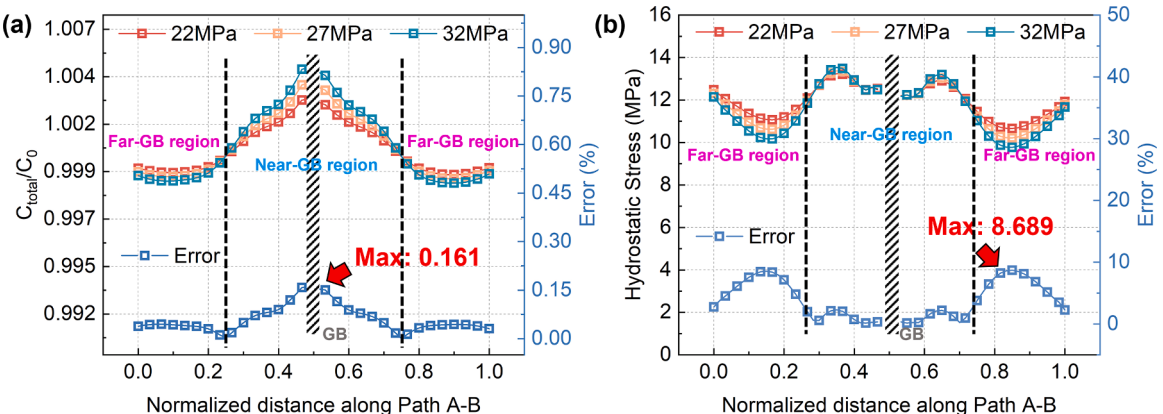


Fig. A.1. The dependence of hydrogen transportation and stress on g_{HP} : (a) relative hydrogen concentration; (b) HS.

Appendix B. Energy dependency analysis of hydrogen diffusion behavior in bicrystal model

The relationship between Q_{seg} and γ_{GB} can be derived from Eqs. (19)–(21) as follows:

$$Q_{seg} = -\gamma_{GB} \left(\frac{\hat{a}^2}{\hat{m}} \right) \quad (\text{B.1})$$

where Q_{seg} is in eV and γ_{GB} is in J/m² (1 eV=1.602 × 10⁻¹⁹J).

Firstly, we keep Q_{seg} of GB constant while varying γ_{GB} , and the simulation results in Fig. B.1(a) indicate that γ_{GB} has no effect on the hydrogen segregation behavior at GB region. Secondly, when γ_{GB} is held constant, the simulation reveals that an increase in the absolute value of Q_{seg} slightly raises the hydrogen concentration at GB region, but the effect is minimal (as shown in Fig. B.1(b)). This is due to the concentration gradient between GB region and GI region, where larger Q_{seg} make it more difficult for hydrogen atoms to jump from GB region to GI region. During the diffusion process, the low hydrogen diffusivity of nickel leads to the negligible influence of Q_{seg} on hydrogen detrapping behavior. Subsequently, we calculate the detrapping and intergranular diffusion for three GBs with their respective γ_{GB} and Q_{seg} calculated using Eq. (B.1). The simulation results in Fig. B.1(c), (d) indicate that the trapping effect of GBs is primarily governed by Q_{seg} , while the diffusion of hydrogen along GBs is governed by γ_{GB} . The dashed line in Fig. B.1(d) represents the hydrogen concentration distribution at GBs with γ_{GB} of 0.843, 0.998, and 1.102, as depicted in Fig. 7. These curves exhibit slightly

higher values compared to the calculations for GBs with smaller segregation energies from Eq. (B.1). However, this difference can be disregarded during the diffusion process.

In addition, the dependence of hydrogen concentration distribution on Q_{seg} and γ_{GB} under internal hydrogen condition has also been studied. As shown in Fig. B.2(a), when Q_{seg} is held constant, γ_{GB} has significant influence on the hydrogen concentration within materials. On the other hand, Fig. B.2(b) demonstrates that when γ_{GB} is constant, the hydrogen concentration is not sensitive to the magnitude of Q_{seg} .

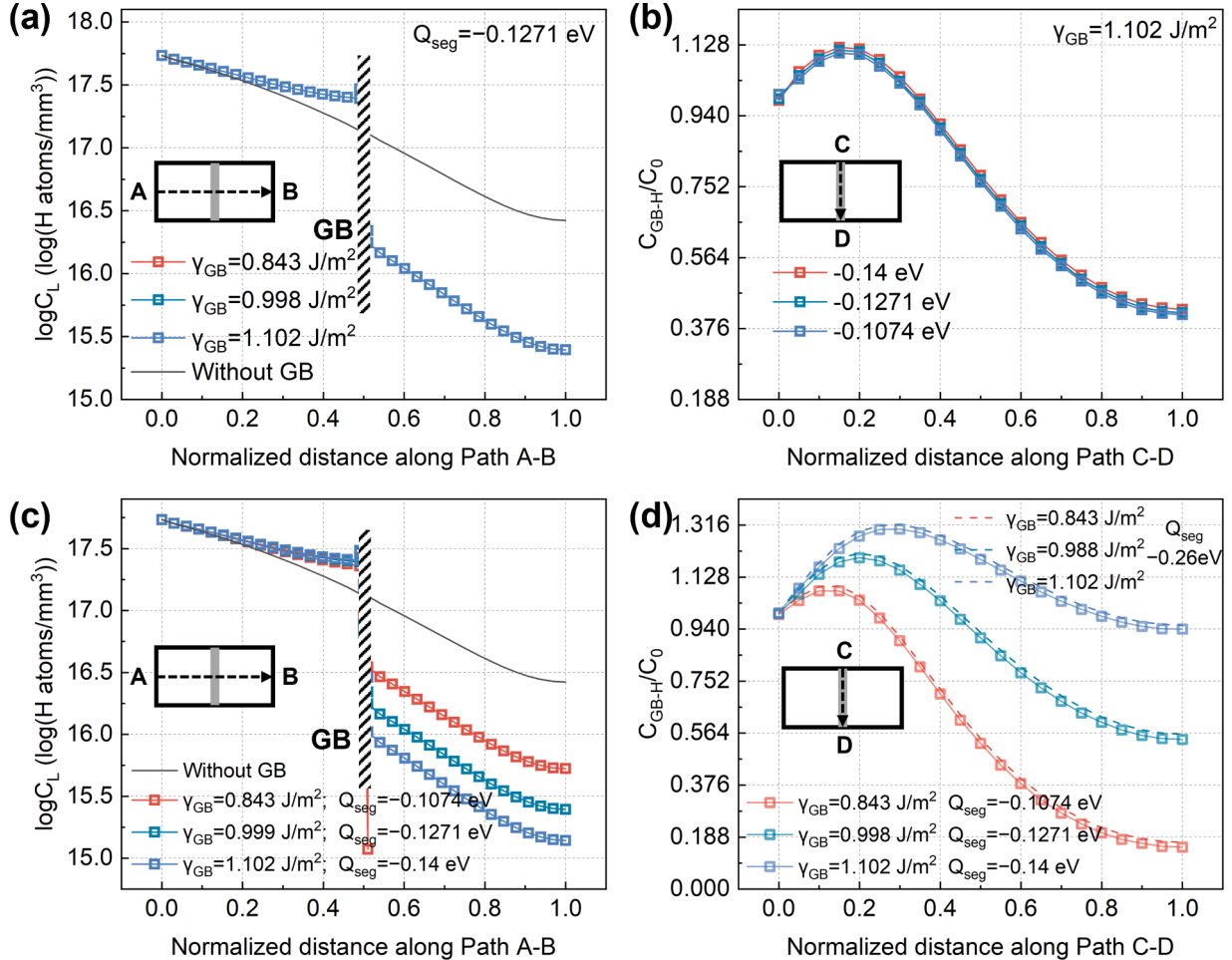


Fig. B.1. The dependence of hydrogen concentration on the segregation energies and GB energies: (a) $\log C_L$ vs. diffusion time (crossing GB); (b) C_{GBH}/C_0 vs. diffusion time (along GB); (c) $\log C_L$ vs. GB; (d) C_{GBH}/C_0 vs. GB.

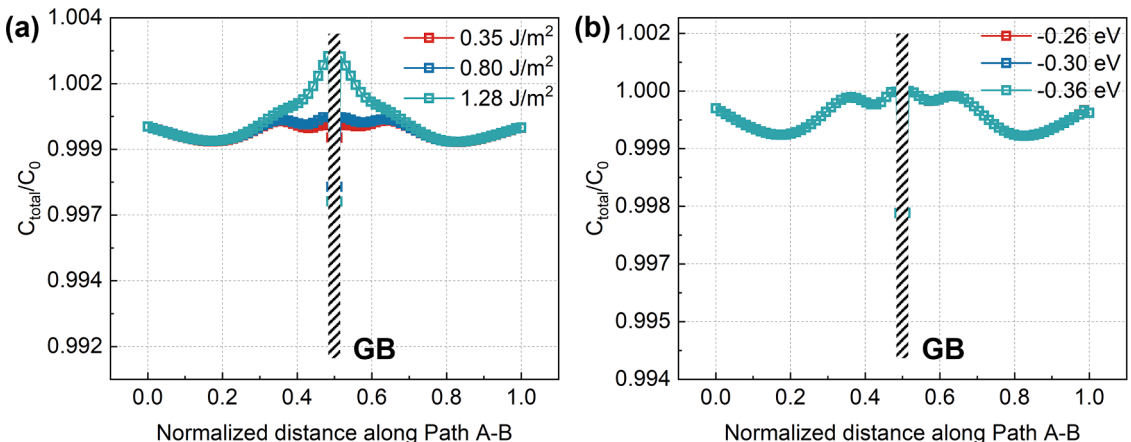


Fig. B.2. The effects of segregation energies and GB energies on the hydrogen diffusion behavior in the internal hydrogen case.**Appendix C. The information and 0 K GB energy of 100-STGBs****Table C1****Table C.1**

The information and 0 K GB energy of 100-STGBs.

CSL&Plane	Tilt Angle (°)	GB energy (J/m ²)	CSL&Plane	Tilt Angle (°)	GB energy (J/m ²)
$\sum 85a(1130)$	8.8	0.843	$\sum 29a(370)$	46.4	1.269
$\sum 61a(1110)$	10.4	0.909	$\sum 73c(5110)$	48.9	1.360
$\sum 41a(190)$	12.7	0.998	$\sum 5(120)$	53.1	1.268
$\sum 25a(170)$	16.3	1.102	$\sum 109a(7130)$	56.6	1.286
$\sum 37a(160)$	18.9	1.152	$\sum 53b(590)$	58.1	1.214
$\sum 13a(150)$	22.6	1.203	$\sum 17a(350)$	61.9	1.146
$\sum 89a(3130)$	26.0	1.247	$\sum 85b(7110)$	64.9	1.104
$\sum 17a(140)$	28.1	1.273	$\sum 13a(230)$	67.4	1.119
$\sum 65b(3110)$	30.5	1.312	$\sum 37a(570)$	71.1	1.103
$\sum 53b(270)$	31.9	1.234	$\sum 25a(340)$	73.7	0.914
$\sum 5(130)$	36.9	1.249	$\sum 65a(790)$	75.8	0.859
$\sum 97c(5130)$	42.1	1.301	$\sum 41a(450)$	77.3	0.816
$\sum 29a(250)$	43.6	1.274	$\sum 101a(9110)$	78.6	0.771

Appendix D. Study of the mesh dependency of the model

To better illustrate the mesh sensitivity of our research results, we varied the number of GB layers from two to four and six, respectively, to analyze the influence of the number of elements through the GB thickness on the results. Additionally, we varied the GB thickness from the previous value of 1 μm to 1.5 μm and 2 μm, respectively, to analyze the effect of GB thickness while keeping the number of GB layers constant at two. Furthermore, we ensured that the layer of elements through GB and GB thickness remained unchanged while varying the mesh size within the GI region to assess the impact of mesh size on the results.

The sensitivities of mesh size and GB thickness were initially analyzed for the hydrogen behavior within the bicrystal model under internal hydrogen conditions. Fig. D.1 depicts the relationship curves of relative hydrogen concentration versus tilt angle along four paths (Fig. 9(a)) with different number of element layers in GB region. Additionally, Fig. D.1 includes the data discrepancies, calculated using Eq. (A.1). From Fig. D.1, it can be observed that the number of element layer in GB region has a small impact on hydrogen transportation, with a maximum difference of 0.1213% along the four paths, which is negligible. Additionally, it is evident that the maximum discrepancy increases with decreasing distance to the GB region. However, the magnitude of the discrepancies is so small that it does not impact the overall trends of the curves. In the near-GB region (such as Fig. D.1(a), (b)), the hydrogen distribution is dominated by HS (Fig. 10(a), (b)), while in the far-GB region (Fig. D.1(c), (d)), the hydrogen distribution is influenced by GB energy (Fig. 10(c), (d)).

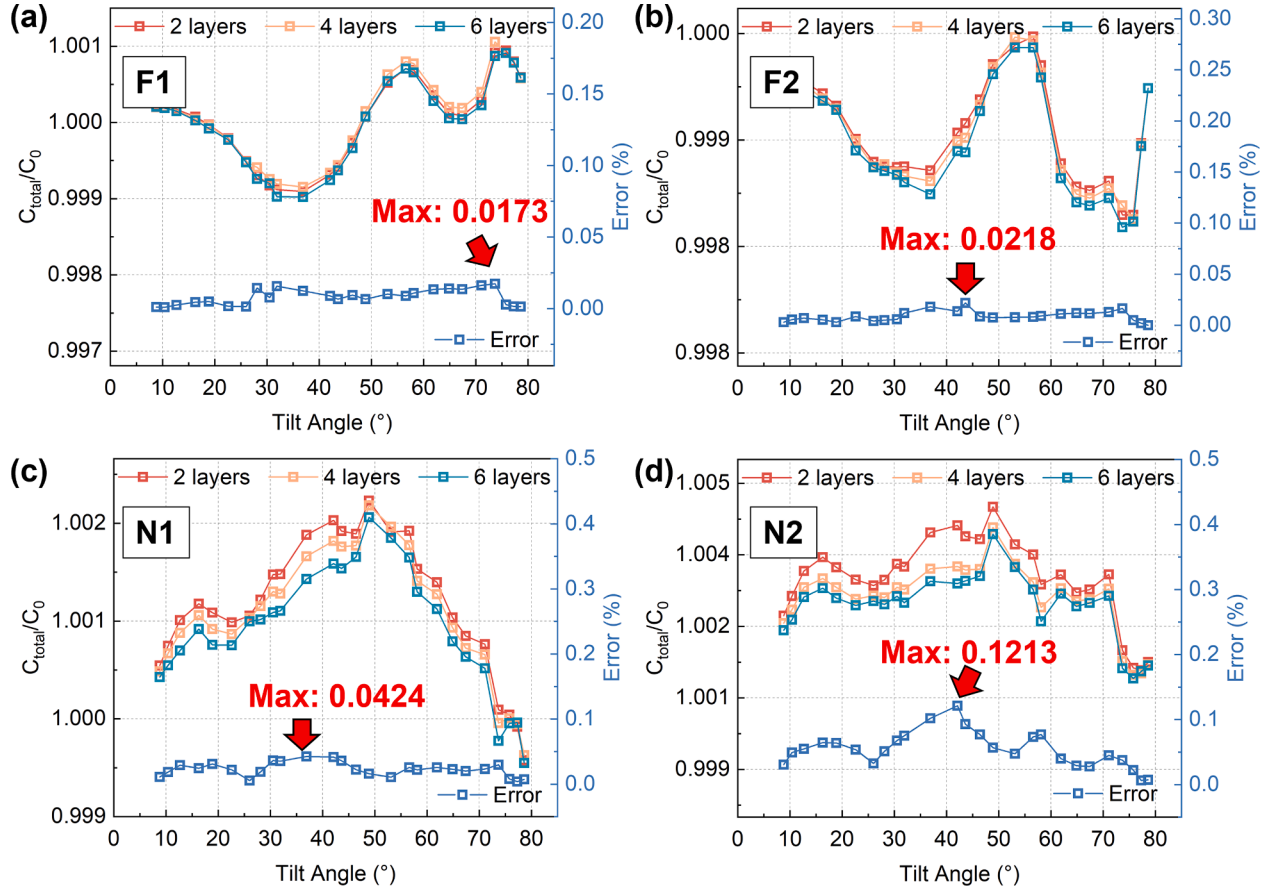


Fig. D.1. The variation of relative hydrogen concentration and errors with tile angle for different mesh layer in GB region: (a) path F1; (b) path F2; (c) path N1; (d) path N2.

The influence of GB thickness on hydrogen diffusion is illustrated in Fig. D.2. The relative hydrogen concentration in the far-GB region shows a slight increase with thinner GBs, while it decreases in the near-GB region, and vice versa. Furthermore, the maximum discrepancy along four paths is only 0.056%. It is also evident from Fig. D.2 that this small difference does not significantly impact the trends obtained in this study, similar to the previous analysis.

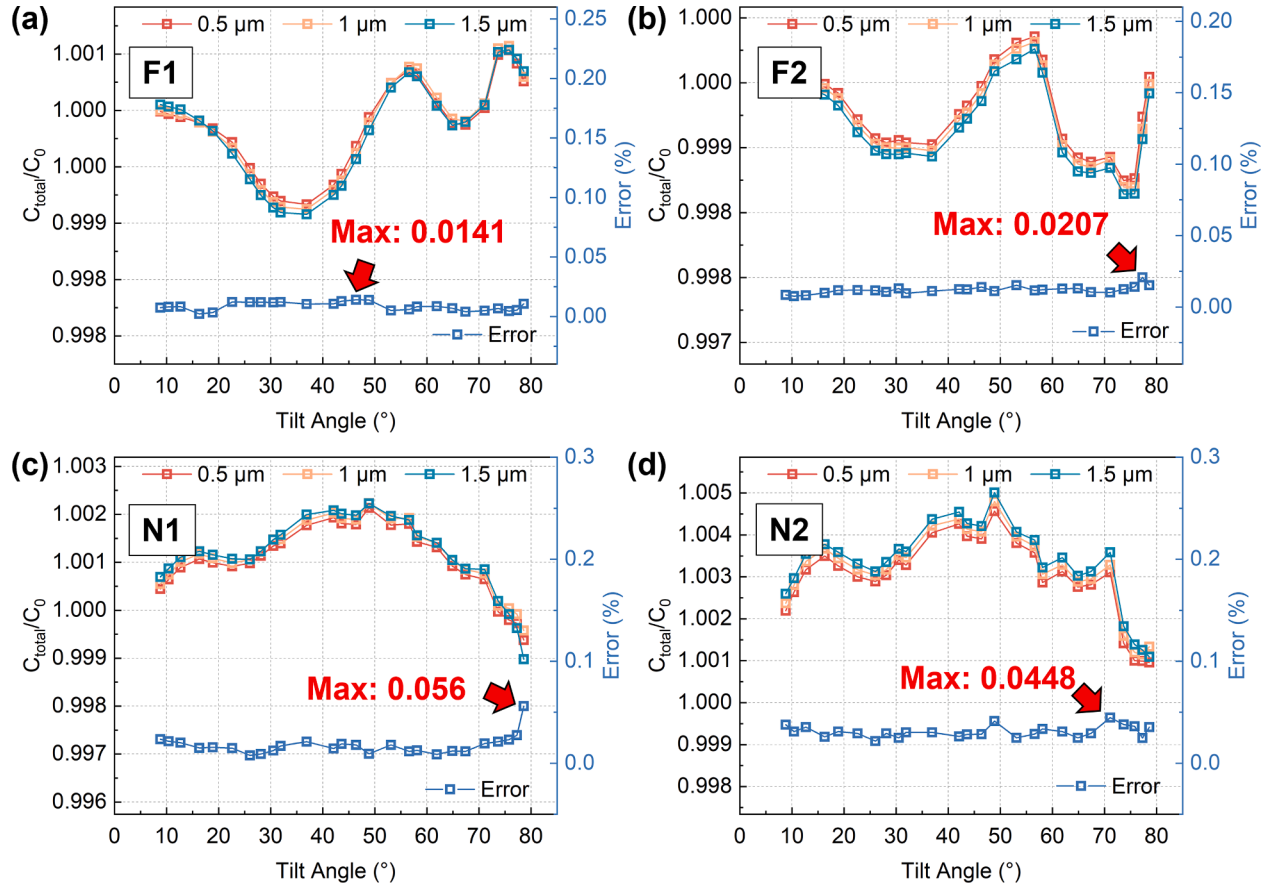


Fig. D.2. The variation of relative hydrogen concentration and errors with tile angle for different thickness of GB region: (a) path F1; (b) path F2; (c) path N1; (d) path N2.

As shown in Fig. D.3, the relationship between the relative hydrogen concentration near $\Sigma 29a$ (250) TGB and the element size of the GI region can be seen. As the element becomes finer, the hydrogen concentration in the near-GB region slightly increases. This is due to the increase in GND density caused by the small element size, which promotes the trapping of hydrogen atoms by GB region. However, the sensitivity of hydrogen concentration to element size is low, as still evident from Fig. D.3, where the maximum difference in relative hydrogen concentration among the curves is less than 0.01, and the discrepancy remains within 1%.

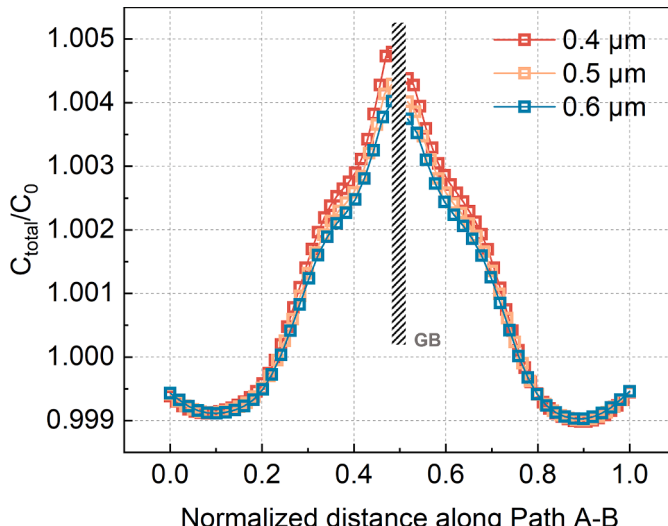


Fig. D.3. The relationship between relative hydrogen concentration and the element size of GI region.

Under external hydrogen conditions, the effects of the number of GB elements and thickness of GB region on hydrogen transportation were also analyzed. The results are shown in Fig. D.4. It can be observed that only variations in GB thickness have a minor influence on hydrogen diffusion perpendicular to the GB (Fig. D.4(a)). This can be attributed to the increased trapping effect of GB region on hydrogen with increasing GB thickness, resulting in a decrease in hydrogen concentration across the GB. The results shown in Fig. D.4(b)–(d) indicate that the hydrogen diffusion perpendicular to GB is insensitive to the number of element layer in GB region. Furthermore, the diffusion along GB is not sensitive to both the number of element layer and thickness of the GB region.

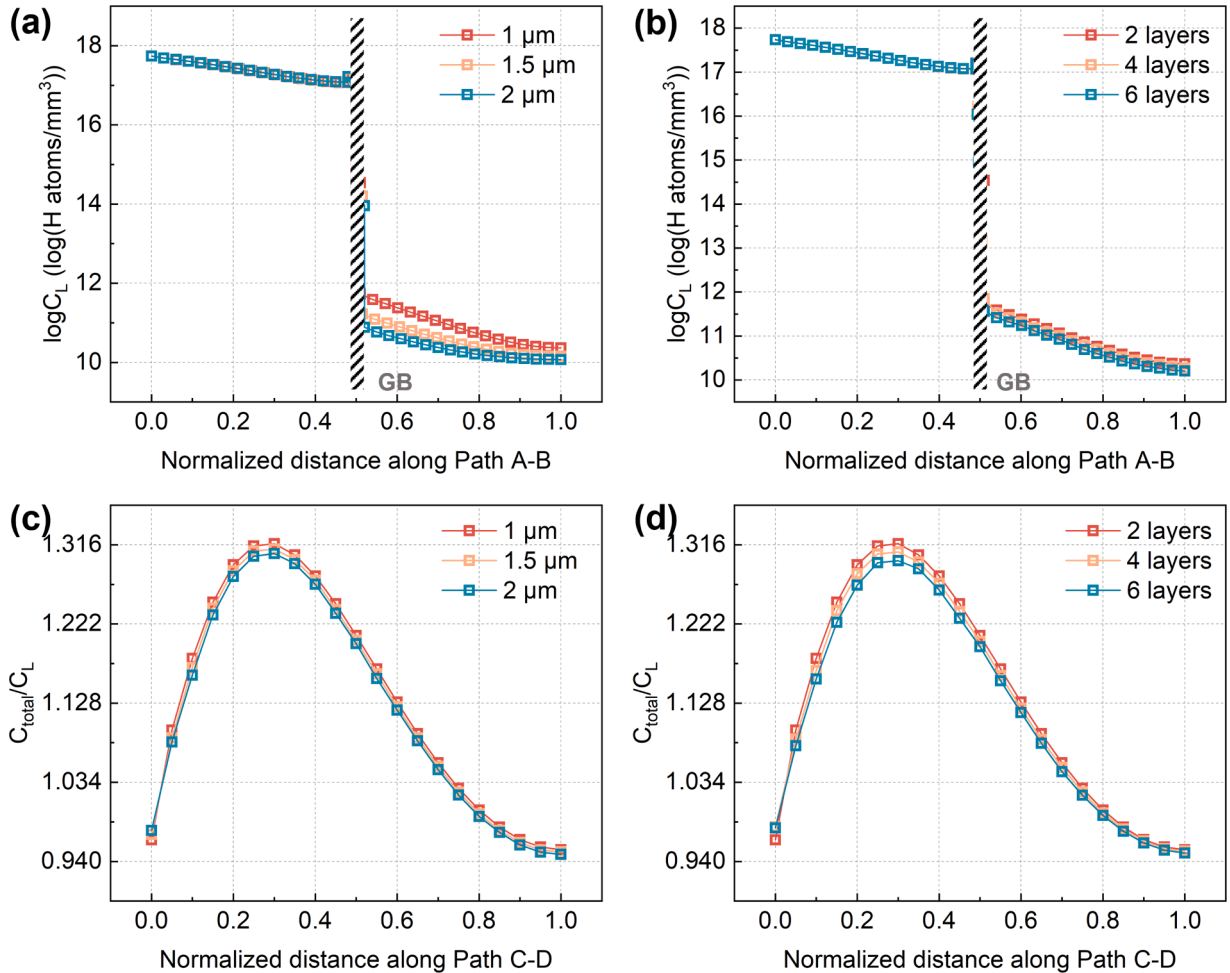


Fig. D.4. The relationship between hydrogen concentration and number of element layer in GB region and GB thickness under external hydrogen conditions: (a) GB thickness-along GB; (b) number of element layer-along GB; (c) GB thickness-across GB; (d) number of element layer-across GB.

To sum up, regardless of whether it is under internal or external hydrogen conditions, the variations in the thickness of GB region and the number of element layer in GB region do not have a significant influence on the hydrogen concentration distribution, thereby hardly affecting the conclusions drawn in this study.

Appendix E. Distribution of hydrogen concentration, HS and their gradient for grain combinations #2 and #3.

[Fig. E1](#), [Fig. E2](#)

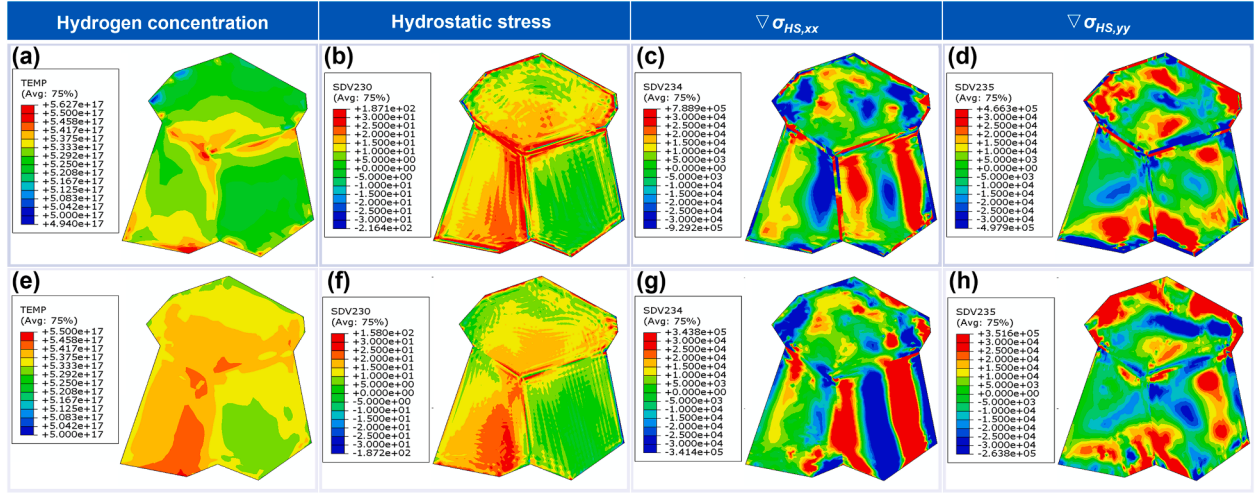


Fig. E.1. Contour plots of hydrogen concentration, HS and its gradient for grain combination #2: (a)-(d): with GB energy; (e)-(f): without GB energy.

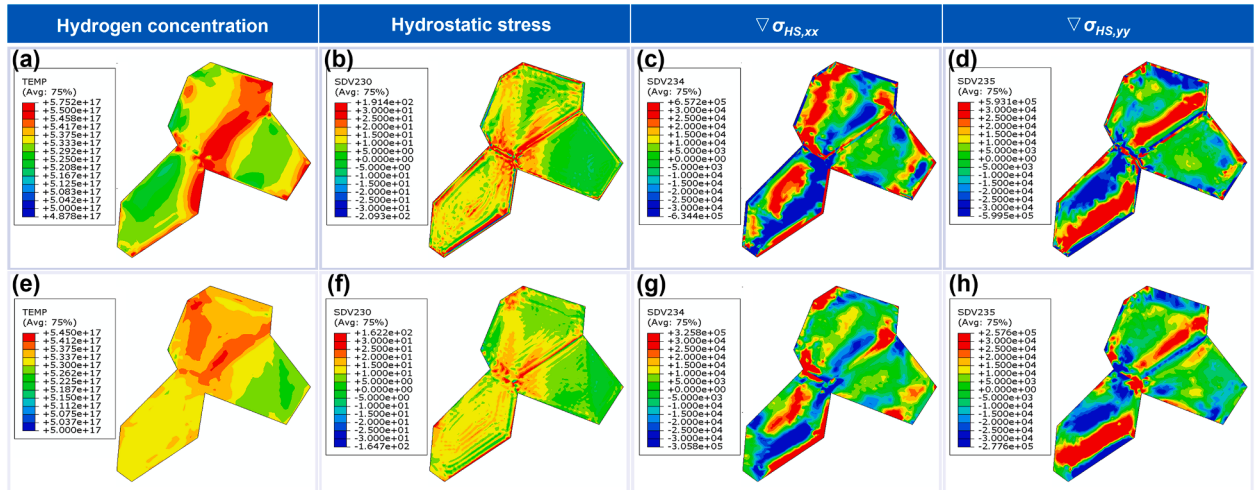


Fig. E.2. Contour plots of hydrogen concentration, HS and its gradient for grain combination #3: (a)-(d): with GB energy; (e)-(f): without GB energy.

Appendix F. Description of the phase-field model

A compact tension (CT) specimen was constructed as depicted in Fig. F.1(a), and a two-dimensional polycrystal model with GB regions consistent with Section 3 was created at the crack tip. The radius of the crack tip is 2.5 μm . And the mesh in the polycrystal region is refined to ensure accuracy and save computational costs. Fig. F.1(b) illustrates the type of each GB region.

During the simulation of crack propagation under external hydrogen conditions, the x and y displacements of edge 2–3 on the sample in Fig. F.1(a) were constrained. The material was assigned an initial hydrogen concentration of 5 wt. ppm to ensure numerical calculation stability. The edges 2–3, 3–4 and 1–4 were subjected to the same boundary conditions of 5 wt. ppm hydrogen concentration. Additionally, the edge 1–2 and the crack surface were exposed to a hydrogen concentration of 100 wt. ppm. A displacement boundary condition was applied to the edge 1–4, with a displacement of 100 μm along the y-axis after the total deformation time. Considering the low diffusivity of hydrogen atoms in nickel, the total deformation time was set to 1×10^7 s. For internal hydrogen conditions, a hydrogen concentration of 100 wt. ppm was applied to the interior and surface of the CT specimen, while the remaining boundary conditions matched those of the external hydrogen conditions. The phase field model involved two key parameters, G_c (the critical energy release rate) and l_c (a length scale parameter). The initial value G_{c0} of G_c for nickel lattice and GB regions are obtained from Valverde-González et al. (2022), and they were 2.5 kJ/m^2 and 0.88 kJ/m^2 , respectively. And the value of l_c used in this study is 0.01 mm. The CPFE parameters and hydrogen diffusion parameters were determined according to the method in Section 4.1.

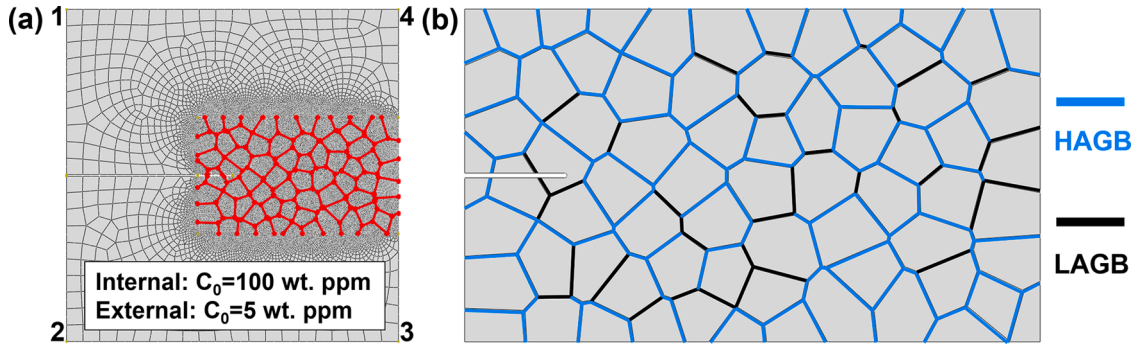


Fig. F.1. Schematic diagram of CT specimen (a) and illustration of GBs (b).

The total potential energy of the material during fracture is given by:

$$\Psi = \int_{\Omega} \left\{ [(1-\varphi)^2 + x_k] (H^e + H^p) + G_c \left(\frac{1}{2l_c} \varphi^2 + \frac{l_c}{2} |\nabla \varphi|^2 \right) \right\} dV \quad (\text{F.1})$$

where H^e and H^p are the elastic strain energy and plastic dissipation energy calculated from the CPFE model, respectively. φ is the damage variable, and x_k is a dimensionless parameter (1e-7 used in this study). The differential of total potential energy in Eq. (F.1) with respect to φ is expressed as follows:

$$\partial\Psi = \int_{\Omega} \left[-2(1-\varphi)(H^e + H^p)\delta\varphi + G_c \left(\frac{1}{l_c} \varphi \delta\varphi + l_c \nabla \varphi \cdot \nabla \delta\varphi \right) \right] dV \quad (\text{F.2})$$

Based on the principle of minimum potential energy, setting Eq. (F.2) equal to zero yields:

$$\int_{\Omega} \left[-2(1-\varphi)(H^e + H^p) + G_c \left(\frac{1}{l_c} \varphi + l_c \nabla \varphi \cdot \nabla \right) \right] dV = 0 \quad (\text{F.3})$$

By discretizing Eq. (F.3), we obtain the out-of-balance force residual with respect to crack phase field:

$$r_i^\varphi = \int_{\Omega} \left[-2(1-\varphi)(H^e + H^p)N_i + G_c \left(\frac{1}{l_c} N_i \varphi + l_c \mathbf{B}_i^T \nabla \varphi \right) \right] dV \quad (\text{F.4})$$

By differentiating Eq. (F.4) with respect to φ , we obtain the consistent tangent stiffness matrix:

$$K_i^\varphi = \frac{\partial r_i^\varphi}{\partial \varphi} = \int_{\Omega} \left\{ \left[2(H^e + H^p) + \frac{G_c}{l_c} \right] N_i N_j + G_c l_c \mathbf{B}_i^T \mathbf{B}_j \right\} dV \quad (\text{F.5})$$

Therefore, based on Eq. (F.4) and Eq. (F.5), the Newton-Raphson algorithm can be applied to solve the phase-field model.

It should be noted that hydrogen may lead to a reduction in the G_c of the materials. Therefore, G_c can be expressed as (Martínez-Pañeda et al., 2018):

$$G_c = G_{c0}(1 - \chi \theta_C) \quad (\text{F.6})$$

where θ_C is the hydrogen coverage, and χ is a dimensionless parameter (0.41 for nickel).

The hydrogen coverage is calculated from the hydrogen concentration obtained from the hydrogen diffusion model described in Section 2.2:

$$\theta_C = \frac{C_{total}}{C_{total} + \exp\left(-\frac{\Delta G_b^0}{RT}\right)} \quad (\text{F.7})$$

where ΔG_b^0 is the activation energy Q_B for the lattice within the GI region, and $(Q_B - Q_{seg})$ within the GB region.

References

- Abdolvand, H., 2019. Progressive modelling and experimentation of hydrogen diffusion and precipitation in anisotropic polycrystals. Int. J. Plast. 116, 39–61. <https://doi.org/10.1016/j.ijplas.2018.12.005>.
- Abraham, D.P., Altstetter, C.J., 1994. The effect of hydrogen on the yield and flow stress of an austenitic stainless steel. Metall. Mater. Trans. A 26, 2849–2858. <https://doi.org/10.1007/BF02669643>.
- Alvaro, A., Thue Jensen, I., Kheradmand, N., Løvvik, O.M., Olden, V., 2015. Hydrogen embrittlement in nickel, visited by first principles modeling, cohesive zone simulation and nanomechanical testing. Int. J. Hydrog. Energy 40, 16892–16900. <https://doi.org/10.1016/j.ijhydene.2015.06.069>.

- Anahid, M., Samal, M.K., Ghosh, S., 2011. Dwell fatigue crack nucleation model based on crystal plasticity finite element simulations of polycrystalline titanium alloys. *J. Mech. Phys. Solids* 59, 2157–2176. <https://doi.org/10.1016/j.jmps.2011.05.003>.
- Arnaudov, N., Kolyshkin, A., Weihe, S., 2020. Micromechanical modeling of fatigue crack initiation in hydrogen atmosphere. *Mech. Mater.* 149, 103557 <https://doi.org/10.1016/j.mechmat.2020.103557>.
- Arora, A., Kumar, R., Mahajan, D.K., 2019. *In-situ* study of the effect of hydrogen on fatigue crack initiation in polycrystalline nickel. *Procedia Struct. Integr.* 14, 790–797. <https://doi.org/10.1016/j.prostr.2019.07.057>.
- Arsenlis, A., Parks, D.M., 2002. Modeling the evolution of crystallographic dislocation density in crystal plasticity. *J. Mech. Phys. Solids* 50, 1979–2009. [https://doi.org/10.1016/S0022-5096\(01\)00134-X](https://doi.org/10.1016/S0022-5096(01)00134-X).
- Ashby, M.F., 1970. The deformation of plastically non-homogeneous materials. *Philos. Mag.* 21, 399–424. <https://doi.org/10.1080/14786437008238426>.
- Barrera, O., Tarleton, E., Tang, H.W., Cocks, A.C.F., 2016. Modelling the coupling between hydrogen diffusion and the mechanical behaviour of metals. *Comput. Mater. Sci.* 122, 219–228. <https://doi.org/10.1016/j.commatsci.2016.05.030>.
- Bayrakdar Ates, E., Calik, E., 2023. Public awareness of hydrogen energy: a comprehensive evaluation based on statistical approach. *Int. J. Hydrot. Energy* 48, 8756–8767. <https://doi.org/10.1016/j.ijhydene.2022.12.070>.
- Biglari, F.R., Nikbin, K.M., 2015. A diffusion driven carburisation combined with a multiaxial continuum creep model to predict random multiple cracking in engineering alloys. *Eng. Fract. Mech.* 146, 89–108. <https://doi.org/10.1016/j.engfracmech.2015.07.057>.
- Birnbaum, H.K., Sofronis, P., 1994. Hydrogen-enhanced localized plasticity—a mechanism for hydrogenrelated fracture. *Mater. Sci. Eng. A* 176, 191–202. [https://doi.org/10.1016/0921-5093\(94\)90975-X](https://doi.org/10.1016/0921-5093(94)90975-X).
- Boniszewski, T., Smith, G.C., 1963. The influence of hydrogen on the plastic deformation ductility, and fracture of nickel in tension. *Acta Metall.* 11, 165–178. [https://doi.org/10.1016/0001-6160\(63\)90209-8](https://doi.org/10.1016/0001-6160(63)90209-8).
- Castelluccio, G.M., McDowell, D.L., 2017. Mesoscale cyclic crystal plasticity with dislocation substructures. *Int. J. Plast.* 98, 1–26. <https://doi.org/10.1016/j.ijplas.2017.06.002>.
- Cecere, D., Giacomazzi, E., Ingenito, A., 2014. A review on hydrogen industrial aerospace applications. *Int. J. Hydrot. Energy* 39, 10731–10747. <https://doi.org/10.1016/j.ijhydene.2014.04.126>.
- Chandra, S., Samal, M.K., Kapoor, R., Chavan, V.M., 2020. Simulation of bicrystal deformation including grain boundary effects: atomistic computations and crystal plasticity finite element analysis. *Comput. Mater. Sci.* 179, 109641 <https://doi.org/10.1016/j.commatsci.2020.109641>.
- Chen, Y.S., Lu, H.Z., Liang, J.T., Rosenthal, A., Liu, H.W., Sneddon, G., McCarroll, I., Zhao, Z.Z., Li, W., Guo, A.M., Cairney, J.M., 2020. Observation of hydrogen trapping at dislocations, grain boundaries, and precipitates. *Science* 367, 171–175. <https://doi.org/10.1126/science.aaz0122>.
- Claeys, L., Knockaert, V., Depover, T., De Graeve, I., Verbeken, K., 2020. Critical assessment of the evaluation of thermal desorption spectroscopy data for duplex stainless steels: a combined experimental and numerical approach. *Acta Mater.* 186, 190–198. <https://doi.org/10.1016/j.actamat.2019.12.055>.
- Cui, T.C., Shang, J., Hua, Z.L., Peng, W.Z., Shi, J.F., Xu, P., Gu, C.H., 2021. A coupled cohesive modeling approach for predicting fractures in low alloy steel under high-pressure hydrogen gas. *Int. J. Hydrot. Energy* 46, 2702–2715. <https://doi.org/10.1016/j.ijhydene.2020.10.064>.
- Darken, L.S., Smith, R.P., 1949. Behavior of hydrogen in steel during and after immersion in acid. *Corrosion* 5, 1–16. <https://doi.org/10.5006/0010-9312-5.1.1>.
- Davis, S.J., Lewis, N.S., Shaner, M., Aggarwal, S., Arent, D., Azevedo, I.L., Benson, S.M., Bradley, T., Brouwer, J., Chiang, Y.M., Clack, C.T.M., Cohen, A., Doig, S., Edmonds, J., Fennell, P., Field, C.B., Hannegan, B., Hodge, B.M., Hoffert, M.I., Ingersoll, E., Jaramillo, P., Lackner, K.S., Mach, K.J., Mastrandrea, M., Ogden, J., Peterson, P.F., Sanchez, D.L., Sperling, D., Stagner, J., Trancik, J.E., Yang, C.J., Caldeira, K., 2018. Net-zero emissions energy systems. *Science* 360, 1419. <https://doi.org/10.1126/science.aas9793>.
- Di Stefano, D., Mrovec, M., Elsässer, C., 2015. First-principles investigation of hydrogen trapping and diffusion at grain boundaries in nickel. *Acta Mater.* 98, 306–312. <https://doi.org/10.1016/j.actamat.2015.07.031>.
- Díaz, A., Alegre, J.M., Cuesta, I.I., 2016. Coupled hydrogen diffusion simulation using a heat transfer analogy. *Int. J. Mech. Sci.* 115-116, 360–369. <https://doi.org/10.1016/j.actamat.2015.07.031>.
- Díaz, A., Cuesta, I.I., Martínez-Pañeda, E., Alegre, J.M., 2019. Analysis of hydrogen permeation tests considering two different modelling approaches for grain boundary trapping in iron. *Int. J. Fract.* 223, 17–35. <https://doi.org/10.48550/arXiv.1912.02525>.
- Djurukic, M.B., Bakic, G.M., Sijacki Zeravcic, V., Sedmak, A., Rajcic, B., 2019. The synergistic action and interplay of hydrogen embrittlement mechanisms in steels and iron: localized plasticity and decohesion. *Eng. Fract. Mech.* 216, 106528 <https://doi.org/10.1016/j.ijhydene.2020.10.064>.
- Elmukashfi, E., Tarleton, E., Cocks, A.C.F., 2020. A modelling framework for coupled hydrogen diffusion and mechanical behaviour of engineering components. *Comput. Mech.* 66, 189–220. <https://doi.org/10.1007/s00466-020-01847-9>.
- Farukh, F., Zhao, L.G., Barnard, N.C., Whittaker, M.T., McColvin, G., 2018. Computational modelling of full interaction between crystal plasticity and oxygen diffusion at a crack tip. *Theor. Appl. Fract. Mech.* 96, 707–719. <https://doi.org/10.1016/j.tafmec.2017.10.010>.
- Han, F.B., Tang, B., Kou, H.C., Li, J.S., Feng, Y., 2015. Experiments and crystal plasticity finite element simulations of nanoindentation on Ti-6Al-4V alloy. *Mater. Sci. Eng. A* 625, 28–35. <https://doi.org/10.1016/j.msea.2014.11.090>.
- Fernández-Sousa, R., Betegón, C., Martínez-Pañeda, E., 2020. Analysis of the influence of microstructural traps on hydrogen assisted fatigue. *Acta Mater.* 199, 253–263. <https://doi.org/10.1016/j.actamat.2020.08.030>.
- Franciosi, P., Berveiller, M., Zaoui, A., 1980. Latent hardening in copper and aluminium single crystals. *Acta Metall.* 28, 273–283. [https://doi.org/10.1016/0001-6160\(80\)90162-5](https://doi.org/10.1016/0001-6160(80)90162-5).
- Fu, H.H., Benson, D.J., Meyers, M.A., 2001. Analytical and computational description of effect of grain size on yield stress of metals. *Acta Mater.* 49, 2567–2582. [https://doi.org/10.1016/S1359-6454\(01\)00062-3](https://doi.org/10.1016/S1359-6454(01)00062-3).
- Gonzalez, D., Simonovski, I., Withers, P.J., Quinta da Fonseca, J., 2014. Modelling the effect of elastic and plastic anisotropies on stresses at grain boundaries. *Int. J. Plast.* 61, 49–63. <https://doi.org/10.1016/j.ijplas.2014.03.012>.
- Haouala, S., Segurado, J., Llorca, J., 2018. An analysis of the influence of grain size on the strength of FCC polycrystals by means of computational homogenization. *Acta Mater.* 148, 72–85. <https://doi.org/10.1016/j.actamat.2018.01.024>.
- Harrison, L., 1961. Influence of dislocations on diffusion kinetics in solids with particular reference to the alkali halides. *Trans. Faraday Soc.* 57, 1191–1199. <https://doi.org/10.1039/TF9615701191>.
- Huang, Q., Zhao, Q., Zhou, H., Yang, W., 2022. Misorientation-dependent transition between grain boundary migration and sliding in FCC metals. *Int. J. Plast.* 159, 103466 <https://doi.org/10.1016/j.ijplas.2022.103466>.
- Huang, S., Chen, D., Song, J., McDowell, D.L., Zhu, T., 2017. Hydrogen embrittlement of grain boundaries in nickel: an atomistic study. *npj Comput. Mater.* 3, 28. <https://doi.org/10.1038/s41524-017-0031-1>.
- Ilin, D.N., Kutsenko, A.A., Tanguy, D., Olive, J.M., 2016. Effect of grain boundary trapping kinetics on diffusion in polycrystalline materials: hydrogen transport in Ni. *Modell. Simul. Mater. Sci. Eng.* 24, 035008 <https://doi.org/10.1088/0965-0393/24/3/035008>.
- Ilin, D.N., Saintier, N., Olive, J.M., Abgrall, R., Aubert, I., 2014. Simulation of hydrogen diffusion affected by stress-strain heterogeneity in polycrystalline stainless steel. *Int. J. Hydrot. Energy* 39, 2418–2422. <https://doi.org/10.1016/j.ijhydene.2013.11.065>.
- Jiang, D.E., Carter, E.A., 2004. First principles assessment of ideal fracture energies of materials with mobile impurities: implications for hydrogen embrittlement of metals. *Acta Mater.* 52, 4801–4807. <https://doi.org/10.1016/j.actamat.2004.06.037>.
- Johnson, H.H., 1973. Hydrogen embrittlement. *Science* 179, 228–230. <https://doi.org/10.1126/science.179.4070.228.d>.
- Keller, C., Hug, E., Habraken, A.M., Duchene, L., 2012. Finite element analysis of the free surface effects on the mechanical behavior of thin nickel polycrystals. *Int. J. Plast.* 29, 155–172. <https://doi.org/10.1016/j.ijplas.2011.08.007>.
- Koyama, M., Yamasaki, D., Nagashima, T., Tasan, C.C., Tsuzaki, K., 2017. *In situ* observations of silver-decoration evolution under hydrogen permeation: effects of grain boundary misorientation on hydrogen flux in pure iron. *Scr. Mater.* 129, 48–51. <https://doi.org/10.1016/j.scriptamat.2016.10.027>.
- Kumar, R., Meena, D., Mahajan, D.K., 2019. Modelling of fatigue crack initiation in hydrogen charged polycrystalline nickel. *Procedia Struct. Integr.* 14, 668–675. <https://doi.org/10.1016/j.prostr.2019.05.083>.

- Li, K.D., Li, J.S., Tang, B., Wang, W.Y., Chen, F.L., Zhang, M.Q., Fan, J.K., Zhong, H., 2021. Experimental and simulation analysis of residual topography dominated deformation mechanism of nanoindentation: a case study of Inconel 625 superalloy. *J. Mater. Res. Technol.* 13, 1521–1533. <https://doi.org/10.1016/j.jmrt.2021.05.054>.
- Li, X.F., Li, Q.Z., Wang, T., Zhang, J., 2019. Hydrogen-assisted failure of laser melting additive manufactured IN718 superalloy. *Corros. Sci.* 160, 108171 <https://doi.org/10.1016/j.corsci.2019.108171>.
- Li, Y.Z., Huang, M.X., 2021. A dislocation-based flow rule with succinct power-law form suitable for crystal plasticity finite element simulations. *Int. J. Plast.* 138, 102921 <https://doi.org/10.1016/j.ijplas.2020.102921>.
- Liu, K., Sluiter, M.H.F., 2023. Stresses at grain boundaries: the maximum incompatibility stress in an infinitely extended elastic bicrystal under uniaxial loading. *Scr. Mater.* 234, 115570 <https://doi.org/10.1016/j.scriptamat.2023.115570>.
- Lu, X., Depover, T., Johnsen, R., 2022a. Evaluation of hydrogen diffusion and trapping in nickel Alloy 625 by thermal desorption spectroscopy. *Int. J. Hydrog. Energy* 47, 31673–31683. <https://doi.org/10.1016/j.ijhydene.2022.07.094>.
- Lu, X., Wang, D., Johnsen, R., 2022b. Hydrogen diffusion and trapping in nickel-based alloy 625: an electrochemical permeation study. *Electrochim. Acta* 421, 140477. <https://doi.org/10.1016/j.electacta.2022.140477>.
- Lufrano, J., Sofronis, P., 1996. Numerical analysis of the interaction of solute hydrogen atoms with the stress field of a crack. *Int. J. Solids Struct.* 33, 1709–1723. [https://doi.org/10.1016/0020-7683\(95\)00119-0](https://doi.org/10.1016/0020-7683(95)00119-0).
- Lufrano, J., Sofronis, P., Birnbaum, H.K., 1996. Modeling of hydrogen transport and elastically accommodated hydride formation near a crack tip. *J. Mech. Phys. Solids* 44, 179–205. [https://doi.org/10.1016/0022-5096\(95\)00075-5](https://doi.org/10.1016/0022-5096(95)00075-5).
- Lufrano, J., Sofronis, P., Symons, D., 1998. Hydrogen transport and large strain elastoplasticity near a notch in alloy X-750. *Eng. Fract. Mech.* 59, 827–845. [https://doi.org/10.1016/S0013-7944\(97\)00142-2](https://doi.org/10.1016/S0013-7944(97)00142-2).
- Lynch, S.P., 1988. Environmentally assisted cracking: overview of evidence for an adsorption-induced localised-slip process. *Acta Metall.* 36, 2639–2661. [https://doi.org/10.1016/0001-6160\(88\)90113-7](https://doi.org/10.1016/0001-6160(88)90113-7).
- Lynch, S.P., 1989. Metallographic contributions to understanding mechanisms of environmentally assisted cracking. *Metallography* 23, 147–171. [https://doi.org/10.1016/0026-0800\(89\)90016-5](https://doi.org/10.1016/0026-0800(89)90016-5).
- Lynch, S.P., 2009. Comments on ‘‘A unified model of environment-assisted cracking’’. *Scr. Mater.* 61, 331–334. <https://doi.org/10.1016/j.scriptamat.2009.02.031>.
- Ma, Z.X., Xiong, X.L., Su, Y.J., 2021. Study on hydrogen segregation at individual grain boundaries in pure nickel by scanning Kelvin probe force microscopy. *Mater. Lett.* 303, 130528. <https://doi.org/10.1016/j.matlet.2021.130528>.
- Ma, Z.X., Xiong, X.L., Zhang, L.N., Zhang, Z.H., Yan, Y., Su, Y.J., 2018. Experimental study on the diffusion of hydrogen along individual grain boundaries in nickel. *Electrochim. Commun.* 92, 24–28. <https://doi.org/10.1016/j.elecom.2018.05.012>.
- Mai, H.L., Cui, X.Y., Scheiber, D., Romaner, L., Ringer, S.P., 2021. An understanding of hydrogen embrittlement in nickel grain boundaries from first principles. *Mater. Des.* 212, 110283 <https://doi.org/10.1016/j.matdes.2021.110283>.
- Martinez-Mardones, J., Worner, C., Walgraef, D., 2000. Materials Instabilities (World Scientific). 10.1142/4384.
- Martínez-Pañeda, E., Golahmar, A., Niordson, C.F., 2018. A phase field formulation for hydrogen assisted cracking. *Comput. Methods Appl. Mech. Eng.* 342, 742–761. <https://doi.org/10.1016/j.cma.2018.07.021>.
- Maugh, T.H., 1972. Hydrogen: synthetic fuel of the future. *Science* 178, 849–852. <https://www.jstor.org/stable/1734906>.
- McCarroll, I.E., Lin, Y.C., Rosenthal, A., Yen, H.W., Cairney, J.M., 2022. Hydrogen trapping at dislocations, carbides, copper precipitates and grain boundaries in a dual precipitating low-carbon martensitic steel. *Scr. Mater.* 221, 114934 <https://doi.org/10.1016/j.scriptamat.2022.114934>.
- McNabb, A., Foster, P.K., 1963. A new analysis of diffusion of hydrogen in iron and ferritic steels. *Trans. Metall. Soc. AIME* 227, 618–627.
- Mehler, H., 2007. Diffusion in Solids: Fundamentals, Methods, Materials, Diffusion-Controlled Process. Heidelberg, Berlin.
- Miresmaeili, R., Saintier, N., Notsu, H., Olive, J.M., Kanayama, H., 2010. One-way coupled crystal plasticity-hydrogen diffusion simulation on artificial microstructure. *J. Comput. Sci. Technol.* 4, 105–120. <https://doi.org/10.1299/jcst.4.105>.
- Moghadam, M.M., Rickman, J.M., Harmer, M.P., Chan, H.M., 2015. The role of boundary variability in polycrystalline grain-boundary diffusion. *J. Appl. Phys.* 117, 045311 <https://doi.org/10.1063/1.4906778>.
- Moghaddam, M.G., Achuthan, A., Bednarzyk, B.A., Arnold, S.M., Pineda, E.J., 2017. Grain size-dependent crystal plasticity constitutive model for polycrystal materials. *Mater. Sci. Eng. A* 703, 521–532. <https://doi.org/10.1016/j.msea.2017.07.087>.
- Murakami, Y., Matsuoka, S., 2010. Effect of hydrogen on fatigue crack growth of metals. *Eng. Fract. Mech.* 77, 1926–1940. <https://doi.org/10.1016/j.engfracmech.2010.04.012>.
- Nagumo, M., Takai, K., 2019. The predominant role of strain-induced vacancies in hydrogen embrittlement of steels: overview. *Acta Mater.* 165, 722–733. <https://doi.org/10.1016/j.actamat.2018.12.013>.
- Nye, J.F., 1953. Some geometrical relations in dislocated crystals. *Acta Metall.* 1, 153–162. [https://doi.org/10.1016/0001-6160\(53\)90054-6](https://doi.org/10.1016/0001-6160(53)90054-6).
- Ogawa, Y., Takakuwa, O., Okazaki, S., Funakoshi, Y., Matsuoka, S., Matsunaga, H., 2020. Hydrogen-assisted fatigue crack-propagation in a Ni-based superalloy 718, revealed via crack-path crystallography and deformation microstructures. *Corros. Sci.* 174, 108814 <https://doi.org/10.1016/j.corsci.2020.108814>.
- Oh, C.S., Kim, Y.J., Yoon, K.B., 2010. Coupled analysis of hydrogen transport using ABAQUS. *J. Solid Mech. Mater. Eng.* 4, 908–917. <https://doi.org/10.1299/jjmm.4.908>.
- Ohaeri, E., Eduok, U., Szpunar, J., 2018. Hydrogen related degradation in pipeline steel: a review. *Int. J. Hydrog. Energy* 43, 14584–14617. <https://doi.org/10.1016/j.ijhydene.2018.06.064>.
- Olden, V., Thaulow, C., Johnsen, R., Østby, E., Berstad, T., 2008. Application of hydrogen influenced cohesive laws in the prediction of hydrogen induced stress cracking in 25%Cr duplex stainless steel. *Eng. Fract. Mech.* 75, 2333–2351. <https://doi.org/10.1016/j.engfracmech.2007.09.003>.
- Olmsted, D.L., Foiles, S.M., Holm, E.A., 2009. Survey of computed grain boundary properties in face-centered cubic metals: I. Grain boundary energy. *Acta Mater.* 57, 3694–3703. <https://doi.org/10.1016/j.actamat.2009.04.007>.
- Orlani, R.A., 1970. The diffusion and trapping of hydrogen in steel. *Acta Metall.* 18, 147–157. [https://doi.org/10.1016/0001-6160\(70\)90078-7](https://doi.org/10.1016/0001-6160(70)90078-7).
- Oudriss, A., Creus, J., Bouthatte, J., Savall, C., Peraudeau, B., Feaugas, X., 2012. The diffusion and trapping of hydrogen along the grain boundaries in polycrystalline nickel. *Scr. Mater.* 66, 37–40. <https://doi.org/10.1016/j.scriptamat.2011.09.036>.
- Page, D.E., Varela, K.F., Johnson, O.K., Fullwood, D.T., Homer, E.R., 2021. Measuring simulated hydrogen diffusion in symmetric tilt nickel grain boundaries and examining the relevance of the Borisov relationship for individual boundary diffusion. *Acta Mater.* 212, 116882 <https://doi.org/10.1016/j.actamat.2021.116882>.
- Pauš, P., Kratochvíl, J., Beneš, M., 2013. A dislocation dynamics analysis of the critical cross-slip annihilation distance and the cyclic saturation stress in fcc single crystals at different temperatures. *Acta Mater.* 61, 7917–7923. <https://doi.org/10.1016/j.actamat.2013.09.032>.
- Peirce, D., Asaro, R.J., Needleman, A., 1983. Material rate dependence and localized deformation in crystalline solids. *Acta Metall.* 31, 1951–1976. [https://doi.org/10.1016/0001-6160\(83\)90014-7](https://doi.org/10.1016/0001-6160(83)90014-7).
- Pfeil, L.B., 1926. The effect of occluded hydrogen on the tensile strength of iron. *Proc. R. Soc. Lond. Ser. A* 112, 182–195. <https://doi.org/10.1098/rspa.1926.0103>.
- Ramasubramaniam, A., Itakura, M., Ortiz, M., Carter, E.A., 2011. Effect of atomic scale plasticity on hydrogen diffusion in iron: quantum mechanically informed and on-the-fly kinetic Monte Carlo simulations. *J. Mater. Res.* 23, 2757–2773. <https://doi.org/10.1557/JMR.2008.0340>.
- Renner, E., Gaillard, Y., Richard, F., Amiot, F., Delobelle, P., 2016. Sensitivity of the residual topography to single crystal plasticity parameters in Berkovich nanoindentation on FCC nickel. *Int. J. Plast.* 77, 118–140. <https://doi.org/10.1016/j.ijplas.2015.10.002>.
- Roters, F., Eisenlohr, P., Hantcherli, L., Tjahjanto, D.D., Bieler, T.R., Raabe, D., 2010. Overview of constitutive laws, kinematics, homogenization and multiscale methods in crystal plasticity finite-element modeling: theory, experiments, applications. *Acta Mater.* 58, 1152–1211. <https://doi.org/10.1016/j.actamat.2009.10.058>.
- Schebler, G., 2010. On the mechanics of the hydrogen interaction with single crystal plasticity. University of Illinois at Urbana-Champaign, Master Thesis. <http://hdl.handle.net/2142/18223>.

- Shiga, M., Yamaguchi, M., Kaburaki, H., 2003. Structure and energetics of clean and hydrogenated Ni surfaces and symmetrical tilt grain boundaries using the embedded-atom method. *Phys. Rev. B* 68, 245402. <https://doi.org/10.1103/PhysRevB.68.245402>.
- Singh, V., Kumar, R., Charles, Y., Mahajan, D.K., 2022. Coupled diffusion-mechanics framework for simulating hydrogen assisted deformation and failure behavior of metals. *Int. J. Plast.* 157, 103392 <https://doi.org/10.1016/j.ijplas.2022.103392>.
- Sofronis, P., McMeeking, R.M., 1989. Numerical analysis of hydrogen transport near a blunting crack tip. *J. Mech. Phys. Solids* 37, 317–350. [https://doi.org/10.1016/0022-5096\(89\)90002-1](https://doi.org/10.1016/0022-5096(89)90002-1).
- Solanki, K.N., Tschopp, M.A., Bhatia, M.A., Rhodes, N.R., 2012. Atomistic investigation of the role of grain boundary structure on hydrogen segregation and embrittlement in α -Fe. *Metall. Mater. Trans. A* 44, 1365–1375. <https://doi.org/10.1007/s11661-012-1430-z>.
- Song, J., Curtin, W.A., 2011. A nanoscale mechanism of hydrogen embrittlement in metals. *Acta Mater.* 59, 1557–1569. <https://doi.org/10.1016/j.actamat.2010.11.019>.
- Song, J., Curtin, W.A., 2013. Atomic mechanism and prediction of hydrogen embrittlement in iron. *Nat. Mater.* 12, 145–151. <https://doi.org/10.1038/nmat3479>.
- Taha, A., Sofronis, P., 2001. A micromechanics approach to the study of hydrogen transport and embrittlement. *Eng. Fract. Mech.* 68, 803–837. [https://doi.org/10.1016/S0013-7944\(00\)00126-0](https://doi.org/10.1016/S0013-7944(00)00126-0).
- Takakuwa, O., Yamabe, J., Matsunaga, H., Furuya, Y., Matsuoka, S., 2017. Comprehensive understanding of ductility loss mechanisms in various steels with external and internal hydrogen. *Metall. Mater. Trans. A* 48, 5717–5732. <https://doi.org/10.1007/s11661-017-4323-3>.
- Tehranchi, A., Curtin, W.A., 2017. Atomistic study of hydrogen embrittlement of grain boundaries in nickel: I. Fracture. *J. Mech. Phys. Solids* 101, 150–165. <https://doi.org/10.1016/j.jmps.2017.01.020>.
- Tehranchi, A., Zhou, X., Curtin, W.A., 2020. A decohesion pathway for hydrogen embrittlement in nickel: mechanism and quantitative prediction. *Acta Mater.* 185, 98–109. <https://doi.org/10.1016/j.actamat.2019.11.062>.
- Tondro, A., Abdolvand, H., 2021. Quantifying hydrogen concentration in the vicinity of zirconium hydrides and deformation twins. *J. Mech. Phys. Solids* 148, 104287. <https://doi.org/10.1016/j.jmps.2020.104287>.
- Tondro, A., Abdolvand, H., 2022. On the effects of texture and microstructure on hydrogen transport towards notch tips: a CPFE study. *Int. J. Plast.* 152, 103234. <https://doi.org/10.1016/j.ijplas.2022.103234>.
- Tondro, A., Taherijam, M., Abdolvand, H., 2023. Diffusion and redistribution of hydrogen atoms in the vicinity of localized deformation zones. *Mech. Mater.* 177, 104544 <https://doi.org/10.1016/j.mechmat.2022.104544>.
- Valverde-González, A., Martínez-Pañeda, E., Quintanas-Corominas, A., Reinoso, J., Paggi, M., 2022. Computational modelling of hydrogen assisted fracture in polycrystalline materials. *Int. J. Hydrog. Energy* 47, 32235–32251. <https://doi.org/10.1016/j.ijhydene.2022.07.117>.
- Watson, J.W., Meshii, M., Shen, Y.Z., 1988. Effect of cathodic charging on the mechanical properties of aluminum. *Metall. Mater. Trans. A* 19, 2299–2304. <https://doi.org/10.1007/BF02645053>.
- West, A.J., Louthan, M.R., 1982. Hydrogen effects on the tensile properties of 21-6-9 stainless steel. *Metall. Mater. Trans. A* 13, 2049–2058. <https://doi.org/10.1007/BF02645950>.
- Yagodzinsky, Y., Saukkonen, T., Tuomisto, F., Barannikova, S., Hnninen, H., 2008. Effect of hydrogen on plastic strain localization in single crystals of nickel and austenitic stainless steel. In: *Proceedings of the International Hydrogen Conference*, pp. 97–104.
- Yao, J., Chaoon, J.R., 1991. Experimental studies of grain boundary diffusion of hydrogen in metals. *Acta Metall. Mater.* 39, 119–126. [https://doi.org/10.1016/0956-7151\(91\)90333-V](https://doi.org/10.1016/0956-7151(91)90333-V).
- Yu, H.Y., Olsen, J.S., Olden, V., Alvaro, A., He, J.Y., Zhang, Z.L., 2017. Cohesive zone simulation of grain size and misorientation effects on hydrogen embrittlement in nickel. *Eng. Fail. Anal.* 81, 79–93. <https://doi.org/10.1016/j.engfailanal.2017.07.027>.
- Yuan, S.L., Zhu, Y.X., Zhao, L., Liang, S., Huang, M.S., Li, Z.H., 2022. Key role of plastic strain gradient in hydrogen transport in polycrystalline materials. *Int. J. Plast.* 158, 103409 <https://doi.org/10.1016/j.ijplas.2022.103409>.
- Zhang, M.Q., Li, J.S., Tang, B., Wang, W.Y., Li, K.D., Zhang, T.L., Wang, D., Kou, H.C., 2022. Quantification of α phase strengthening in titanium alloys: crystal plasticity model incorporating α/β heterointerfaces. *Int. J. Plast.* 158, 103444 <https://doi.org/10.1016/j.ijplas.2022.103444>.
- Zhao, L., Xu, L.Y., Nikbin, K., 2017. Predicting failure modes in creep and creep-fatigue crack growth using a random grain/grain boundary idealised microstructure meshing system. *Mater. Sci. Eng. A* 704, 274–286. <https://doi.org/10.1016/j.msea.2017.08.035>.
- Zheng, J.Y., Ran, J.Q., Fu, M.W., 2022. Constitutive modeling of multiscale polycrystals considering grain structures and orientations. *Int. J. Mech. Sci.* 216, 106992 <https://doi.org/10.1016/j.ijmecsci.2021.106992>.
- Zhou, X.Y., Zhu, J.H., Wu, H.H., 2021. Molecular dynamics studies of the grain-size dependent hydrogen diffusion coefficient of nanograined Fe. *Int. J. Hydrog. Energy* 46, 5842–5851. <https://doi.org/10.1016/j.ijhydene.2020.11.131>.